8-24-2012

Process parameter modeling for nanocrystalline ceria based thin films prepared via aerosol jet printing

Sundaresan Balasubramanian

Process Parameter Modeling For Nanocrystalline Ceria Based Thin Films Prepared Via Aerosol Jet Printing

Sundaresan Balasubramanian

Thesis submitted to the Faculty of the

Rochester Institute of Technology

in partial fulfillment of the requirements for the degree of

Master of Science

in

Industrial Engineering

Thesis Committee

Dr. Denis Cormier

Dr. Marcos Esterman

Department of Industrial and Systems Engineering
Kate Gleason College of Engineering

August 24, 2012
Rochester, New York

DEPARTMENT OF INDUSTRIAL AND SYSTEMS ENGINEERING

KATE GLEASON COLLEGE OF ENGINEERING

ROCHESTER INSTITUTE OF TECHNOLOGY

ROCHESTER, NEW YORK

CERTIFICATE OF APPROVAL

August 24, 2012

M.S. DEGREE THESIS

The M.S. Degree Thesis of Sundaresan Balasubramanian
has been examined and approved by the
Thesis Committee as satisfactory for the
Thesis requirement for the
Master of Science degree

Approved by

Dr. Denis Cormier, Thesis Advisor

Dr. Marcos Esterman, Committee Member

Process Parameter Modeling For Nanocrystalline Ceria Based Thin Films Prepared Via Aerosol Jet Printing

Sundaresan Balasubramanian

Abstract

Solid Oxide Fuel Cells (SOFCs) are becoming a popular choice for meeting energy requirements of the present day due to their high efficiency and reformation capabilities. SOFCs are made of ceramic oxides with well-defined physical and thermal properties enabling a high operating temperature range (600-800°C). Efficiency of a SOFC is typically well represented by its output voltage. Resistances across various components of the SOFC viz. anode, electrolyte and cathode diminish the maximum output voltage thus directly affecting the efficiency of the fuel cell. Each of the layers in a SOFC has generic as well as specific requirements warranting specialized fabrication processes. While such processes are many in number, they face limitations on size of the particles usable for the process, cost, ability to create graded porosity, thickness, etc. The main thrust of this work is the employment of a novel direct-write tool, namely the Optomec Aerosol Jet deposition system for fabricating the electrolyte layer of a SOFC that addresses some of the practical limitations of traditional SOFC fabrication techniques.

While Optomec's Aerosol Jet deposition technique has been employed in several applications including printed electronics, a structured approach to identifying process parameters for printing materials was not found in literature. This work identifies and models process parameters significant to the deposition of nanocrystalline ceria with thickness of the deposited layer as response variable through design of experiments. Initial feasibility tests determined printability of the test ink and established a working range for the desired process parameters under investigation. A full factorial design with five factors and two levels was executed as the screening design. Three of five factors were determined as significant from the screening experiments. A regression equation was generated with the three significant terms from screening. Validation runs executed indicated lack of curvature within the design space for the significant parameters.

Coefficients of terms from the regression equation were updated after regression analysis of a higher order design of experiments with three levels and the three significant parameters from screening. The updated regression equation provides a model with a reduced standard error and better fit of residuals as compared to the model from screening. A brief study on drying methods post-deposition and its impact on the quality of the printed film is also presented in this work.

Dedicated to

the quintessential graduate student –

may your quest for knowledge and free pizza never cease.

Acknowledgements

I would like to start by thanking my family for the countless sacrifices they have made to better my life. I thank my mother and sister for their unconditional love and infinite patience with me even as I struggled with my studies in the aftermath of my father's sudden demise last year. I thank my late father for instilling in me the values of patience and honesty which I hold paramount. I also wish to thank my uncle, Mr. Narayanan Balakrishnan for his guidance throughout my academic career and his unwavering faith in me.

Words cannot adequately describe the feeling of gratitude I wish to express to my advisor, Dr. Denis Cormier. His calmness and positivity has been a great source of inspiration to me and our research team at RIT. This thesis and my Masters degree would not have been made possible if not for his inputs and ideas. I feel privileged to have worked with him on the HeteroFoaM research project which has opened new interesting research windows for me. I would like to thank Dr. Marcos Esterman for his inputs on my experimental designs and analyses which was an indispensable part of this work. I also wish to express my gratefulness to Dr. Kyle Brinkman at the Savannah River National Labs for his help with EDX analysis, to Lyn Irving from Cerion Energy, Rochester for her help with ink formulations and to Richard Hailstone from the Chester F. Carlson Center for Imaging Sciences at RIT for his help with SEM imaging.

I owe much more than a simple thank you (and a few dollars paid for my meals) to my friend and fellow graduate student, Anuj Datar. I am certain that our legendary discussions on music, graduation and post-graduation plans, 9gag, residuals analysis and rapid prototyping will one day become content for college level textbooks. I wish him the very best in life. I also thank my awesome friends Manoj, Sai, Visweshwar,

Vijay, Anirudh, Srinivas and Ajay for their amazing company. And I tip my hat to Sheldon Cooper, Gregory House, Michael Scofield, Patrick Jane, Dexter Morgan, Eric Cartman and Michael Scott for making college life very enjoyable.

This work was supported by Heterogeneous Functional Materials Center (HeteroFoaM), an Energy Frontier Research Center (ERFC) funded by the U.S. Department of Energy and Office of Basic Energy Sciences under award number DE-SC0001061.

Contents

List of Figures

List of Tables

Chapter 1

Introduction

1.1 Solid Oxide Fuel Cells

Solid Oxide Fuel Cells (SOFCs) are a preferred choice amongst fuel cells for automobile and power generation applications since they have very high efficiencies and operating temperatures. SOFCs use solid ceramic materials as electrolyte which can function at high temperatures (700-1000°C). This high temperature is beneficial for co-generation of electricity and high-grade heat, increasing the overall system efficiency. The performance of a SOFC can be summarized with a graph of the current-voltage characteristics (*i–V* curve). The *i–V* curve represents the voltage output of the fuel cell for a given current output. The power output of the SOFC is given by the product of current and voltage.

$$P = iV \tag{1.1}$$

The current supplied by the SOFC is proportionate to the amount of fuel consumed, since each mole of fuel provides n moles of electrons. Thus, the electric power produced per unit fuel decreases with decrease in the fuel cell voltage. Hence, fuel cell voltage can be considered as a measure of the efficiency of the SOFC. To maintain high efficiency in the SOFC, it is essential that the voltage in the SOFC be maximized. It is difficult to maintain a high voltage in the SOFC under constant current load due to voltage losses.

The actual output voltage that can be obtained from a SOFC is less than the thermodynamically predicted voltage output due to irreversible losses. The greater the current drawn from the cell, the greater are the losses. These losses give the *i–V* plot its characteristic curvature (Figure 1.1). Losses in a SOFC can be classified into three major types:

1. Activation losses
2. Ohmic losses
3. Concentration losses

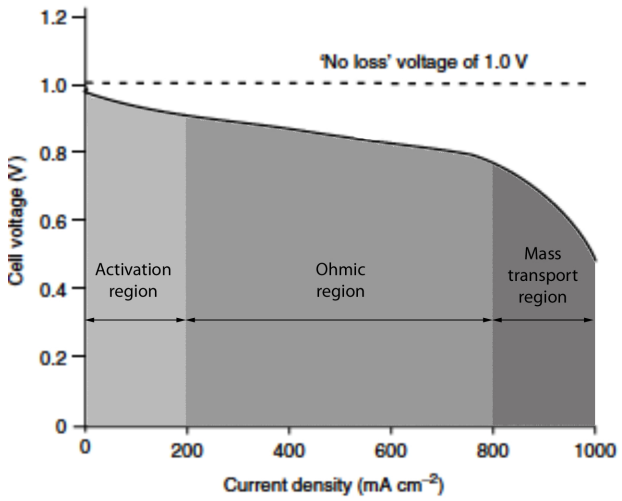

Figure 1.1: Typical *i–V* plot for SOFC [1]

Activation losses occur due to the electrochemical reaction in the SOFC. Losses due to the ionic and electronic conduction constitute Ohmic losses. Lastly, concentration losses occur during mass transport. Activation losses mostly affect the initial part of the *i–V* curve; ohmic losses are apparent in the middle section of the curve and concentration losses are significant in the tail of the *i–V* curve. After considering voltage drops occurring due to the various losses in the SOFC [2], the equation for real voltage output can be written as

$$V = E_{thermo} - \eta_{act} - \eta_{ohmic} - \eta_{conc} \tag{1.2}$$

where,

V = real voltage output of the SOFC

E_{thermo} = thermodynamically predicted voltage output of the SOFC

η_{act} = activation losses occurring due to reaction kinetics

η_{ohmic} = ohmic losses from ionic and electronic conduction

η_{conc} = concentration losses due to mass transport

Activation losses, η_{act} (also called activation overpotential or activation overvoltage), represent the voltage that has to be sacrificed to lower the activation barrier of the electrochemical reaction that generates current in the SOFC. The activation barrier impedes the conversion of the reactants into products (and vice versa) and thus controls the rate of the reaction directly. The rate of electrochemical reaction determines the rate at which current is produced in the SOFC. Thus η_{act} directly affects the overall voltage output of the SOFC, and in turn, the efficiency.

Concentration losses, η_{conc}, occur due to reactant depletion or product clogging at the electrodes and is heavily associated with mass transport. Mass transport in fuel cell electrodes is dominated by diffusion; diffusion limitations in the electrode lead to a limiting current density, j_L. The limiting current density, j_L corresponds to the point where the reactant concentration drops to zero. Convective transport, which occurs in the flow structures of the SOFC refers to the transport of a species by the bulk motion of the fluid. Concentration losses can be minimized by careful consideration of convective transport in the SOFC flow channels.

Charge transport (conduction) in SOFCs is driven by a gradient in voltage. The voltage that is expended to drive conductive charge represents a loss in the efficiency of the SOFC. Known as ohmic overpotential (η_{ohmic} or ohmic losses), this loss generally obey's Ohm's law of conduction,

$$V = iR \tag{1.3}$$

where R is the ohmic resistance of the SOFC. Ohmic resistance of the SOFC, R includes the resistance from the electrodes, electrolyte, the interconnects, etc.

Charge transport in an electrochemical system involves two types of charged species viz., electrons and ions. Both of these charge types must be transported from the electrode in which they are produced to the electrode in which they are consumed to complete the circuit in the electrochemical system. Transport of electrons differs from that of ions, primarily due to the large difference in mass between the two. Since ions have greater mass than electrons, ionic transport is more difficult in SOFCs than electronic transport.

The ohmic losses term from equation 1.2 can be re-written to include both the ionic and electronic components of resistance as follows:

$$\eta_{ohmic} = iR_{ohmic} = i(R_{elec} + R_{ionic}) \tag{1.4}$$

Because ionic transport tends to be more difficult than electronic transport in the SOFC, ionic contribution to resistance R_{ionic}, tends to dominate the overall contribution to resistance. Hence, performance improvements to the fuel cell may be achieved by developing better ion conductors or by reducing R_{ionic}.

Charge transport occurs in response to forces acting on charge carriers. The governing equation for transport can be generalized (for a single dimension) as

$$J_i = \sum_k M_{ik}\, F_k \tag{1.5}$$

where J_i represents a flux of species i, F_k represents the k forces acting on i, and M_{ik}'s are the coupling coefficients between force and flux [2]. In SOFCs, three major driving forces give rise to charge transport viz., electrical driving forces (represented by an electrical potential gradient dV/dx), chemical driving forces (represented by a chemical potential gradient $d\mu/dx$) and mechanical driving forces (represented by a pressure gradient dP/dx). In metal electrodes, the electron charge transport is driven by a voltage gradient;

in the electrolyte, both a concentration gradient and a voltage gradient drive ionic transport. However, in almost all situations, the electrical driving force dominates the ion transport in the SOFC [3]. Considering this, equation 1.5 can be rewritten as

$$j = \sigma \left(\frac{dV}{dx} \right) \tag{1.6}$$

where j represents the charge flux (current density), dV/dx is the electric field that provides the driving force for the charge transport and σ is the conductivity, which is the property of a material to permit flow of charge in response to an electric field. Charge flux through a conducting medium of length L and cross-sectional area A is given by the equation

$$j = \sigma \left(\frac{V}{L} \right) \tag{1.7}$$

Charge flux (or current density) j and current i are related as

$$j = \left(\frac{i}{A} \right) \tag{1.8}$$

Combining equations 1.7 and 1.8, we get

$$V = i \left(\frac{L}{A\sigma} \right) \tag{1.9}$$

This equation is similar to Ohm's law if we consider the term $(L/A\sigma)$ as the resistance R. The voltage V in this equation represents the voltage required to transport charge at a rate given by i and is expended to accomplish charge transport. This loss in voltage arises due to the material's intrinsic resistance (resistivity) to transport of charge (resistivity $\rho = 1/\sigma$)

Equation 1.9 implies that the SOFC resistance depends on the geometry. R_{ohmic} scales with area and hence area specific resistance (ASR) is used to compare fuel cells of different sizes. Since resistance is inversely proportional to area, it is multiplied with the area to make it area independent. ASR is calculated by multiplying the area of a SOFC by its ohmic resistance; its unit is $\Omega \cdot \mathrm{cm}^2$.

$$\mathrm{ASR_{ohmic}} = \mathrm{A_{SOFC}} \cdot R_{ohmic} \tag{1.10}$$

Equation 1.9 can be rewritten in terms of ASR as follows

$$\mathrm{ASR}_{\mathrm{ohmic}} = \left(\frac{L}{\sigma}\right) \tag{1.11}$$

Equation 1.11 implies that the resistance reduces with the length of the conductor, L. Ionic conductivity of SOFCs are much smaller in magnitude as compared to the electronic conductivity and so increasing the ionic conductivity of the electrolyte layer is critical to improving the overall voltage of the SOFC. Materials with better ionic conductivity can be used as electrolyte material at the expense of operating temperature. Reducing the thickness of the electrolyte layer improves the ionic conductivity; however, thickness of the electrolyte layer is limited by practical considerations such as mechanical integrity, non-uniformities, shorting, fuel crossover, etc. For SOFCs, the predicted ultimate thickness for maximizing the electrolyte layer's ionic conductivity (and the overall power density of the SOFC) is in the order of a few tens of nanometers. However, practical limitations mentioned earlier limit the achievable thickness to about 10-100 μm. A brief summary of some of the key concepts discussed in this section is presented below.

1. The maximum voltage that can be obtained from a button cell is limited to a large extent by losses which occur due to the transport of charged species in the fuel cell (ions and electrons). The calculated voltage loss term due to charge transport is similar to Ohm's law. These losses are hence called Ohmic losses.

2. There are two components to Ohmic resistance - ionic and electronic resistance. Since ions are fundamentally heavier than electrons, the ionic component of the Ohmic resistance has greater impact on the overall resistance in a SOFC.

3. Ohmic resistance of a conductor is inversely proportional to its thickness. By this rationale, reducing the thickness of the electrolyte layer in a SOFC reduces its ionic resistance (increases the ionic conductivity of the electrolyte layer).

4. Theoretically, the predicted ultimate thickness for maximizing the ionic conductivity of a SOFC is on the range of a few nanometers. However, due to practical limitations such as mechanical stability, fuel crossover, etc., suggested electrolyte layer thicknesses range from 10–100μm.

1.2 SOFC geometries

Several techniques for fabrication of the SOFC components viz., anode, cathode and electrolyte exist in literature. It is worthwhile to note that in all these techniques, the procedure for fabricating each of the SOFC components is the same; the final SOFC assembly is simply obtained by fabricating the components as layers built successively on top of the previously fabricated (component) layer. It can hence be adequately generalized that most of these methods are applicable to all components in the SOFC viz., anode, cathode and electrolyte. Fabrication processes for SOFCs can be classified into two broad categories viz., gas-phase and wet-type methods. Gas-phase methods include electrochemical vapor deposition, plasma spraying, laser evaporation, reactive magnetron sputtering, etc. [4]. Wet-type methods include tape casting, screen printing, calendering, spin coating, dip coating, etc. [5, 6]. Gas-phase fabrication methods are usually carried out at elevated temperatures and so the active cell material layer that is obtained normally does not require any post-fabrication processing. In contrast, wet-type fabrication methods are performed at room temperature; the green product is then sintered at high temperatures (1400–1700°C) to obtain a reinforced structure capable of being used in stacks. SOFC fabrication approaches may either be particulate or deposition based. Particulate fabrication methods include tape casting, tape calendaring, screen printing, wet spraying, etc. followed by high temperature sintering. In contrast, cell components are fabricated on a support by physical/ chemical processes such as chemical vapor deposition, plasma spraying, dip coating, etc. in the deposition approach [7]. Commonly used SOFC fabrication techniques will be reviewed in Section 1.3.

Geometry of the SOFC is critical for the choice of fabrication technique. SOFC designs can be broadly classified into supported and self-supporting structures. Supported designs require a substrate to mechanically support and stabilize the cell and the stack whereas self-supporting structures depend on the electrode structures for supporting other cell components. Self-supporting structures can be either be electrolyte-supported or electrode supported structures. Common configurations for SOFCs include the tubular configuration (Figure 1.2) developed by Westinghouse, the monolithic design (Figure 1.3) developed by Argonne National Laboratory and the planar design (Figure 1.4) or bipolar plate configuration developed by Siemens [8, 9]. The tubular configuration is said to have better thermal stability compared to the other two designs, but the

monolithic and planar configurations have higher efficiency.

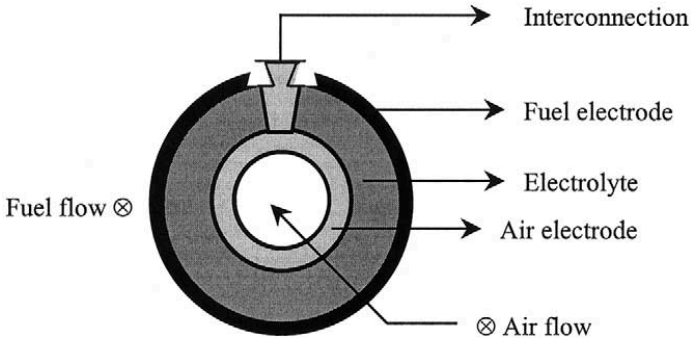

Figure 1.2: Tubular configuration SOFC [8]

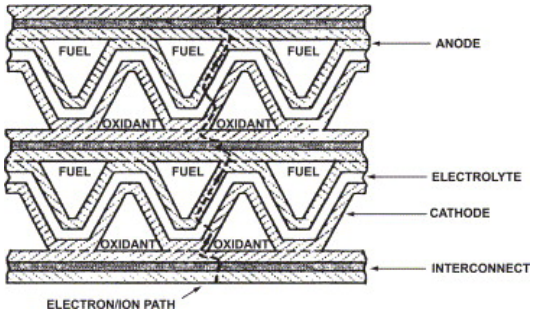

Figure 1.3: Monolithic configuration SOFC [9]

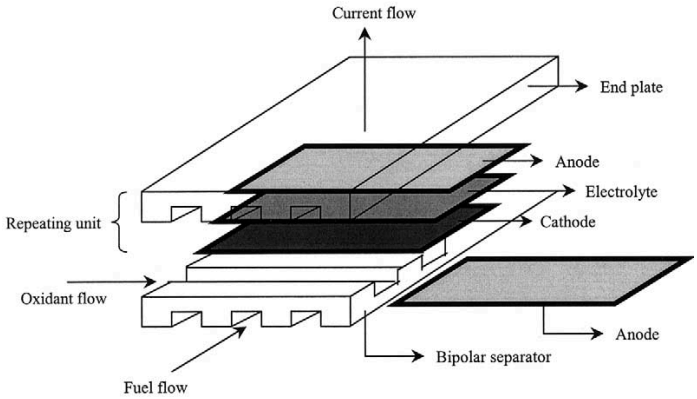

Figure 1.4: Planar configuration SOFC [8]

SOFC fabrication is also limited to a certain degree by the choice of materials. Typically ceramic materials are used for most cell components; these materials do not have particularly good machinability or manufacturability properties. SOFC components have multiple functions to perform and hence materials for those layers have to meet generic as well as specific requirements. Generic requirements for all materials in a SOFC are,

1. Stability at room temperature and elevated temperatures. This includes chemical, morphological, structural and phase components.
2. Compatibility (physical and chemical) with other materials in the structure.
3. High strength and toughness.
4. Similar rate of thermal expansion between layers such as to avoid cracking at elevated temperatures during operation.
5. Good conductivity (electronic and ionic).
6. Easy and inexpensive to fabricate.

In addition to these, each of the layers also have specific requirements. For instance

1. The electrolyte must be sufficiently dense to prevent mixture of gases.
2. The electrode layers have to be sufficiently porous to allow gas transport to the reaction sites.
3. The interconnect material must be gas tight to avoid fuel leakage.
4. The area of contact for the fuel at the reaction sites must be maximized.

Materials for the anode, cathode and interconnect have been elaborately discussed in [10, 11, 12, 13, 14, 15] and have not been included here in the interest of limiting the scope of this review. For the ions to travel through the electrolyte to the fuel side of the cell, the electrolyte must possess good ionic conductivity. Ideally, the electrolyte must be non-porous with a very dense structure such that the reactant gases do not combine with each other. The thickness of the electrolyte must be minimized optimally so as to prevent resistive losses in the cell. It should also be ensured that the electrolyte materials do not react with the cathode materials to produce undesirable insulating phases at the SOFC operating temperature. Some popular materials used in electrolyte fabrication have been discussed in the following paragraphs.

Ideal candidates for the electrolyte include yttria stabilized zirconia (YSZ), samarium doped ceria (SDC), doped bismuth oxide, to name a few. Bismuth oxide (BiO) based materials have high ionic conductivity and operate at temperatures below 800°C but cannot retain their structural integrity at such high temperatures. Lanthanum strontium gallate magnesite (LSGM) and gadolinium doped ceria (GDC) have been reported to exhibit good ionic conductivity at reduced operating temperatures [10].

YSZ has been established as a model electrolyte material due to its outstanding mechanical stability. It stabilizes zirconia into the cubic structure at high operating temperatures and also provides oxygen vacancies. Table 1.1 summarizes the advantages and disadvantages of some of the candidates for electrolyte material.

Table 1.1: Advantages and disadvantages of various electrolyte materials for SOFC [16]

YSZ	GDC	LSGM
Excellent stability (oxidizing and reducing environment)	Good compatibility with cathode materials	Good compatibility with cathode materials
Excellent mechanical stability	Mixed ionic and electronic conductor at low pO_2	Ga-evaporation at low pO_2
High operating life	Low OCV from electronic conduction at low pO_2	Incompatible with NiO
Low ionic conductivity	Mechanical stability	Mechanical stability

1.3 Review of common SOFC fabrication techniques

Tape casting

Tape casting is the most commonly used method for fabricating SOFC components. Tapes of ceramic material are produced from its slurry. The slurry consists of a mixture of the ceramic powder, an ink vehicle and other additives depending on the requirements. A doctor blade evenly spreads a thin layer of material across the tape bed. The layer is allowed to dry before post processing. Freeze tape casting is an advanced tape casting process where an aqueous sol is spread by the doctor blade on a cold substrate maintained at

sub zero temperatures (-40°C). The aqueous solution freezes on the cold substrate and is characterized by nucleation and growth of ice crystals. Freeze drying removes the ice from this layer of deposited material leaving behind a porous part. Required geometries are then blanked out from this sheet of ceramic material [17]. A schematic of the freeze tape casting process is shown in Figure 1.5.

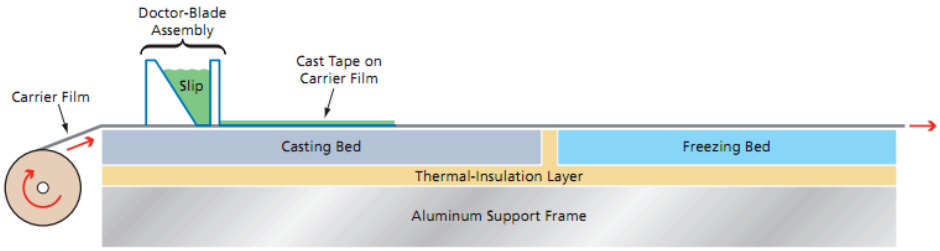

Figure 1.5: Freeze tape casting schematic [17]

Tape calendaring

In tape calendaring process, two or more layers of film are rolled together to create a multi-layer structure. Typically, the individual layers of film are laminated before bring rolled together. These structures are then cut to required size and sintered to form the multi-layered cells (Figure 1.6). [18]

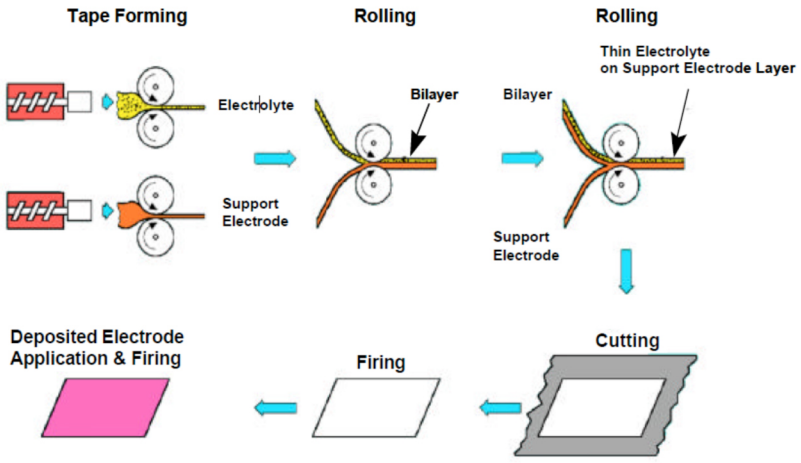

Figure 1.6: Tape calendaring process [18]

Screen printing

Screen printing deposits ink on to the substrate by placing a screen over it and spreading the ink over the screen with a slight pressure. The ink squeezes through the open pores in the screen and gets deposited on the substrate forming a layer of material [19]. Thicknesses around 20 µm can be obtained with screen printed layers (Figure 1.7).

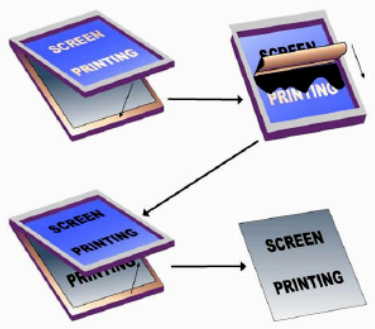

Figure 1.7: Screen printing process [19]

Dip coating

Dip coating is the process of creating a thin film by dipping the substrate in a coating liquid. The dipped substrate is then withdrawn at a controlled speed. Thickness of the film is influenced by the factors such as withdrawal speed, viscosity of the coating liquid, surface tension, etc. Dip coating can produce layer thicknesses of around 20 µm [20]. The thickness of the layer can be increased by repeating the dip coating process after the base layer has dried (Figure 1.8).

Plasma spraying

Plasma spraying is a thermal spray deposition process where material is deposited by introducing the material to a plasma jet. The coating material, usually a powder, is carried by a stream of inert gas into the plasma jet where it is instantaneously heated and propelled towards the substrate (Figure 1.9. Materials with high melting points can be used with plasma spraying due to the inherent high temperature operation of the plasma jet [21].

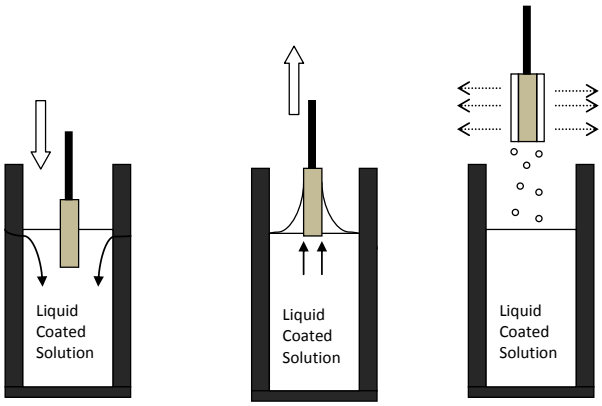

Figure 1.8: Dip coating schematic [20]

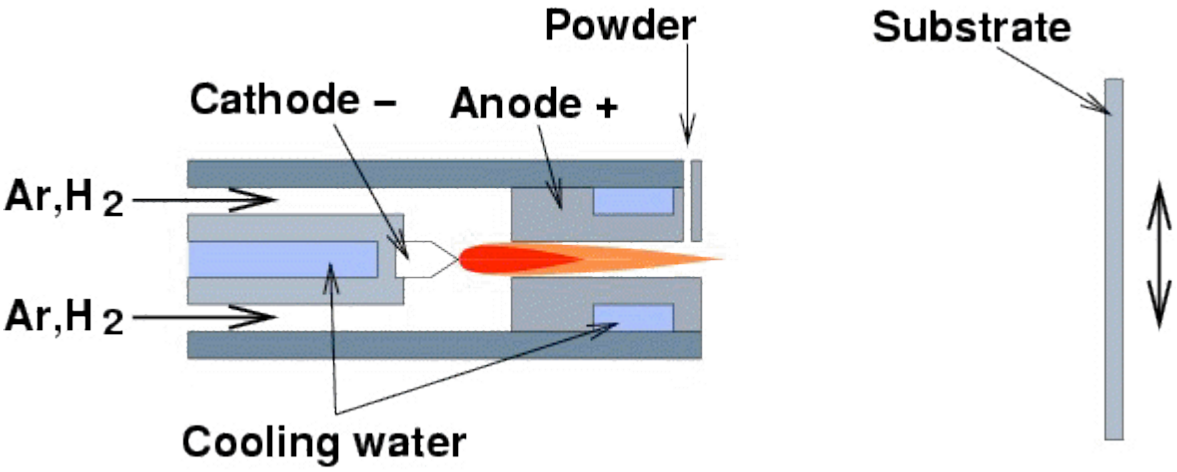

Figure 1.9: Plasma jet spraying process [19]

Spin coating

Spin coating uses centrifugal force to spread a thin layer of film across the substrate. A small amount of liquid material is deposited on to the center of the substrate. This is followed by spinning the substrate at very high speeds (3000–10000 rpm) for a predetermined duration. The solvents are dried off leaving behind a sample with a very small thickness (a few microns) [20]. Repeating this procedure results in a multi-layered structure.

The thickness of the electrolyte layer is typically maintained at around 40 µm. Fabrication methods used include physical vapor deposition (PVD), sputtering, pulsed laser deposition, molecular beam epitaxy (MBE), chemical vapor deposition (CVD), electrochemical vapor deposition (EVD), plasma techniques, etc. PVD and CVD methods are generally not preferred due to their very high setup cost. EVD method offers high purity and a greater level of process control but is also an expensive process. Alternative electrolyte deposition methods include spray coating and dip coating followed by sintering. Colloidal suspensions of YSZ are applied in thin layers of at least 20 µm, using nano-size (5-10 nm) particles in order to meet the critical requirement of low porosity. Table 1.2 presents a qualitative comparison of some of the common fabrication techniques for fuel cell components.

Table 1.2: Summary of SOFC fabrication processes [20]

Process	Grading capability	Cost (time/complexity)	Porosity	Thickness
Tape casting	Poor	High	0-60%	>7 µm
Tape calendaring	Poor	High	N/A	N/A
Screen printing	Poor	Low	0-60%	>8 µm
Spin coating	Yes	Low	0-60%	>1 µm
Dip coating	Poor	High	0-60%	>10 µm
Plasma spraying	Yes	High	5-20%	>Particle size

1.4 Problem statement

Most of the currently employed SOFC fabrication techniques attempt to minimize the thickness of the electrolyte layers; however these processes often have restrictions that limit the scope of their application. Examples of some of these restrictions include requirement for high substrate temperature (700–900°C), complex deposition parameters, cost of the processes, uneven thickness in printed layers, complex procedures for substrate preparation, sintering, etc. YSZ electrolyte layers that are about 10 µm thick have been built on a nickel oxide–yttria stabilized zirconia (NiO–YSZ) substrate through electrophoretic deposition [22].

The ability to tailor the electronic and ionic conductivities by controlling the processing characteristics and the grain size of nano-crystalline oxides, such as cerium oxide (CeO_2) has been studied extensively by Chiang et al. [23] and has been demonstrated by Brinkman et al. [24]. Ceria (cerium dioxide) is being considered as a possible electrolyte material due to its high ionic conductivity and its ability to operate at lower temperatures (around 700°C). In two-phase systems such as barium fluoride (BaF_2) and calcium fluoride (CaF_2), an increase in ionic conductivity was observed with decreasing thickness of layers in a stacked structure [25]. Decreasing grain sizes affect electron concentrations in these systems, leading to increased electronic conductivity, while reduced contribution of perpendicular grain boundaries to bulk ionic defects is responsible for increased ionic conductivity. This results in an increased 'mixed conductivity' that includes both ionic and electronic components. This could lead to oxygen separation in CeO_2 driven solely by the chemical potential gradient of oxygen, without the need for oxygen injection mechanisms often used in zirconia and ceria based electrolyte systems.

Brinkman et al. were able to fabricate CeO_2 layers 500 nm thick via spin coating to study oxygen permeation and oxygen flux properties. The study has also established that nano-crystalline CeO_2 can be used as oxygen separation membrane with grain size being the key design parameter. Sample preparation described in Brinkman et al's work [24] involves the following steps:

1. Porous cerium oxide substrates were prepared by ball milling with 7% ethanol powder for 24 hours and die pressing the powder into pellets of 16mm diameter. These pellets were sintered for 6 hours at 1500°C.

2. To mitigate the problem of sol-gel leakage into the substrate, a layer of cerium oxide was sputter coated onto the polished porous substrate.

3. The ceria sol was deposited by spin coating onto the porous cerium oxide substrates (with the cerium oxide buffer layer) at 3000 rpm for 30 seconds, followed by drying for 3 minutes at 100°Cand pyrolysis for 3 minutes at 350°C. This procedure was repeated ten times before heat-treatment in an air operated furnace. The samples were sintered at 800°C for 30 minutes. This entire procedure was repeated to obtain multi-layer films consisting of 60 sol-gel layers.

4. Thin film development of cerium oxide by sol-gel deposition and sputtering techniques were performed on Pt/Si substrates with rapid thermal annealing to 800°C for 10 minutes in air following film deposition. The final nominal film thickness was about 500 nanometers.

Brinkman et al.'s work is critical to this study for several reasons, the most important of which are his observations on the ionic conductivity of the spin coated nano-scale CeO_2 layer. Initial experiments in Brinkman et al.'s work indicated that sputter coated layers (of about 1 μm thickness) on porous cerium oxide substrates could not prevent leakage of air during oxygen flux measurements. Though the use of a 'blocking layer' to prevent sol-gel leakage into the porous cerium oxide substrates warranted additional resource intensive processing steps in the fabrication sequence, it was reported that the resulting composite structure reduced the solution leakage into the substrate.

Wang et al. [26] have attempted to study the effect of electrolyte thickness on mixed conductivity (electronic and ionic conductivity) on a dense layer of SDC deposited on a substrate of nickel oxide–samarium doped ceria (NiO-SDC), used as an anode material. Wang et al.'s study shows that completed SOFC button cells with an electrolyte layer thickness of about 1.5 μm show elevated power densities with increasing operating temperatures. Brinkman et al.'s work is also key with regards to the processing steps involved in fabricating an electrolyte layer whose thickness is comparable to the grain size in the parent suspension. While being successful in creating layer thicknesses in the nano-scale which most traditional SOFC fabrication techniques are unable to accomplish, Brinkman et al's work involves a large number of processing steps that are resource intensive as well as time consuming.

Sukeshini et al. have reported printing of SOFC electrolyte and cathode layers using Aerosol Jet deposition [27]. They have described deposition of YSZ onto cathode structures of gadolinium doped ceria–lanthanum strontium cobalt ferrite (GDC-LSCF) and made assessments on the feasibility of on-the-fly mixing of individual aerosolized inks in their investigation. An examination of parameters extrinsic to the deposition process such as cathode thickness, solid loading and sintering temperature was also discussed in the study. However, there was no investigation on parameters intrinsic to the Aerosol Jet deposition process in Sukeshini et al.'s work.

This thesis work aims to address the relatively long processing time and complexity of the overall fabrication process employed by Brinkman et al. through use of Optomec's novel Aerosol Jet deposition technology. The Aerosol Jet process is a novel direct write technique that uses a finely collated stream of aerosolized droplets of nano ink for fabrication of a variety of materials such as metals, polymers, ceramics, etc. Aerosol Jet deposition is effective for preparing ceramic films with thicknesses in the order of a few hundreds of nanometers to a few microns. Aerosol Jet deposition is well suited for fabrication of highly dense layers through high rates of deposition. Wang et al. have been able to successfully deposit a dense layer of SDC on a substrate of NiO-SDC (anode) using the Aerosol Jet deposition technique [26]. Electrochemical results presented in Wang et al.'s work illustrate the effect of electrolyte thickness on mixed electronic and ionic conductivity of the printed SDC layer. The major thrust for this work is to establish parameters that will successfully fabricate a layer of electrolyte using the Optomec Aerosol Jet deposition tool and create a process parameter model that will adequately represent printed layer thicknesses through a series of designed experiments.

The remainder of this thesis is organized as follows - Chapter 2 reviews the novel Aerosol Jet deposition technology and briefly touches on the basic steps involved in the fabrication process of the electrolyte layer. Chapter 3 details the experimentation involved in this work such as the feasibility trials, screening experiments and verification runs for process parameter modeling as well as a brief study on the effects of drying methods on cracking in the printed electrolyte layer. Chapter 4 concludes the thesis with a summary of the results and a discussion of some interesting possibilities for future work based on some of the results presented in this work.

Chapter 2

Methodology

Direct writing (DW) is a family of flexible multi-length scale processes for the deposition of functional materials to form simple linear or complex conformal structures on a substrate [28]. Precise quantities of functional and/or structural materials can be deposited onto a substrate at digitally defined co-ordinates. Direct writing techniques differ from conventional RP techniques in the following ways:

1. Width of the deposited tracks range from a few hundreds of nanometers to a few of millimeters.
2. The substrate is an integral part of the final product.
3. Choice of printable materials include metals, polymers, ceramics, living cells, etc.

Section 2.1 presents an overview of the Aerosol Jet deposition process and the mechanism of atomization and deposition. Section 2.2 describes the steps involved in the fabrication of a SOFC layer. Section 2.3 explains briefly the process parameter modeling methodology employed in this study.

2.1 Overview of Aerosol Jet deposition

The Aerosol Jet based direct-write technology developed by Optomec is ideal for fabricating the electrolyte layer because it provides accurate control over deposited track geometry. Aerosol Jet deposition is different from ink-jet printing in the sense that Aerosol Jet deposition uses aerodynamic focusing to deliver accurate

quantities of fluid or nano material formulations [29]. The resulting geometries can have features that are 10 microns or less in width and a few tens of nanometers to several microns in thickness. Advantages of the Aerosol Jet deposition method are as follows:

1. Feature sizes vary between few tens of nanometers to a few microns.
2. Choice of materials available for printing.
3. Wide range of printable viscosities (1–1,000 cP).
4. Room temperature processing.
5. Non-planar printing capability.

Aerosol Jet deposition has been used for deposition of a wide range of materials including metals, ceramics, polymers, etc. Mette and Richter have reported printing 14 μm lines of metallic silver using Aerosol Jet deposition process for metallization of solar cells [30]. Cho et al. have been able to successfully metallic electrodes, a polymer semi-conductor and a dielectric medium for an organic thin film transistor (OTFT) using Aerosol Jet deposition [31]. Akedo has demonstrated deposition of lead zirconate titanate (PZT) using Aerosol Jet deposition [32].

Aerosol Jet deposition begins with the atomization of a source liquid (or nano material formulation) that is refined and densified in a virtual impactor unit. The material stream is then aerodynamically focused using a deposition head that creates an annular sheath gas flow around the aerosolized jet stream to collimate the aerosol. The aerosol jet then exits the material deposition head as a finely focused jet directed at the substrate. The size of the aerosol jet thus exiting the deposition head can be as small as one tenth of the size of the nozzle. The substrate is attached to a computer controlled platen that moves to generate geometric patterns of the deposited material. A 5mm standoff distance allows for deposition on non-planar surfaces.

The Optomec Aerosol Jet system has an atomizing unit, a virtual impacting unit and a nozzle system that deposits material on to the substrate. The ink (or the nano-material formulation) is placed inside the atomizing cup which is sealed air tight with a lid assembly. The lid assembly consists of the atomizer, air conveying shaft and a virtual impactor connection shaft. The atomizer is a threaded hollow cylinder with a hole on the

side and bottom surfaces, connected internally by a micro-machined conduit.

The threaded air conveyor mates with the atomizer and forms an air-tight system by means of an o-ring. When a carrier gas (example: N_2, O_2, etc.) is passed through the atomizer at a given volume, a pressure differential is generated between the side and bottom holes, causing a partial vacuum near the tip of the side hole. Due to capillary action and the pressure gradient, liquid flows up through the bottom hole through the micro machined conduit (see Figure 2.1). When the liquid reaches the side hole in the atomizer where there is a partial vacuum, it is instantly atomized producing sub-micron sized particles suspended in the carrier gas.

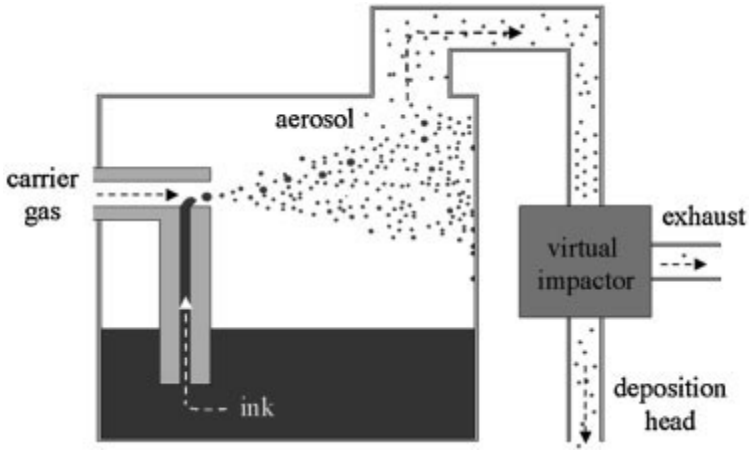

Figure 2.1: Working of the atomizer and virtual impactor unit [30]

The virtual impacting unit densifies the aerosol mist generated in the atomizing chamber by removing excess carrier gas in suspension. The mist enters the deposition head as a fine and dense aerosolized jet. This aerosol jet is surrounded by an annular flowing sheath gas that prevents the aerosol jet from touching the sides of the deposition head in the nozzle assembly (see Figure 2.2). Any accumulation of droplets or aerosol mist on the deposition head leads to rapid material build up in the nozzle tip eventually leading to a clog. Volumetric flows of the carrier gas, sheath gas and the volume of gas to be removed through the virtual impactor are software controlled. The atomizer and the virtual impacting unit have a volumetric flow capacity of up to 2000 ccm while the sheath flow is limited to 200 ccm.

The system is equipped with heating elements in the atomizing unit (a ring heater) and the platen to control the temperature of the deposition material and/or the substrate. There is also a hollow cylindrical tube heater that heats the tube connecting the virtual impactor to the deposition head. Temperatures up to 200°C can be attained in each of the heating units. Heating may be conducive to the deposition process or detrimental depending on the volatility of the liquid and the solid loading fraction in the ink formulation.

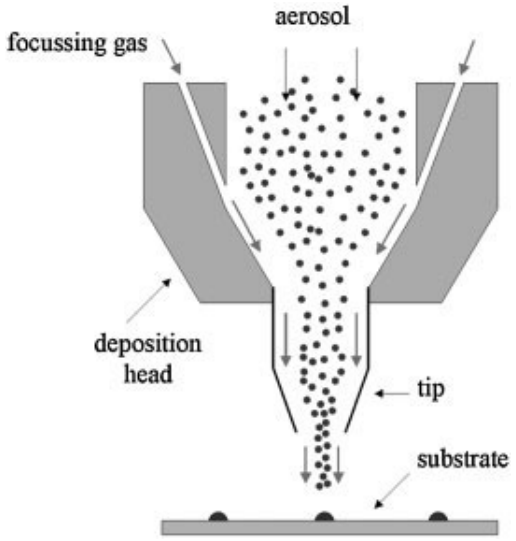

Figure 2.2: Schematic of the deposition head [30]

RIT's Aerosol Jet machine tool is equipped with a 40 mW diode laser that has a spot diameter of approximately 5 µm. The laser can be fired with a maximum current of 2 amps, which translates to a maximum power of about 420 mW. The spot diameter of the laser and it's maximum rated power can provide some degree of localized heating that may be sufficient for thermal post processing for some materials. The platen movement is computer controlled and has a resolution of 0.25 µm enabling precise motion controls for fabricating highly intricate and micron level geometries. The platen can translate at a maximum linear velocity of 100 mm/sec which is suitable for depositing materials at much higher rates. Substrates placed on the platen are held in position by a mild vacuum. Substrate locations can be defined and/or calibrated using an alignment camera while the deposition or heat treatment process is relayed live through the deposition or laser camera.

2.2 SOFC layer fabrication

Fabrication of a layer of material for use in a SOFC is a multi-step operation. The basic steps involved are:

1. Ink preparation
2. Substrate preparation
3. Layer/film deposition
4. Post-deposition sintering

Each of these steps have been described in greater detail in the following sections.

Ink Preparation

The ink required for fabricating the electrolyte layer is created by mixing nano sized powder of the electrolyte material with a suitable ink vehicle such as terpineol, water, ethylene glycol, etc. Co-solvents such as glycerol, disperbyk, etc. may also be added on an as-needed basis depending on the surface chemistry of the substrate. Preliminary mixing is done by hand. The mixture is then homogenized by mixing it in a planetary centrifugal mixer (Thinky mixer ARE-310) for a preset duration of time and speed (rpm). The Thinky mixer processes the dispersion and de-aerates the solution simultaneously. The homogenized ink is transferred into an atomizing cup for further processing on the Optomec machine.

The volume of gas required to atomize a given liquid typically increases with increase in the viscosity of the liquid; the Optomec tool at RIT is best suited for inks that fall in the low to medium viscosity range (1-1000 cP) due to volumetric flow constraints built into the machine. Optomec builds a high volume flow controller to support film deposition of larger areas through a wide area deposition nozzle. Increase in the solid loading fraction of an ink typically entails viscosity of the ink. Due to the printable viscosity range supported by the Optomec tool, it is typically suited well for inks with solid loading fractions between 2 to 30%. Printability of inks also depend on the type of solvent used and behavior of solid particles dispersed in the ink. A comprehensive list of materials that have been successfully deposited with the Optomec machine has been listed in [33].

Substrate preparation

Several types of substrates can be used with the Optomec machine. The primary requirement of the substrate is that the deposited layer of material must adhere to it through cohesive/ adhesive forces. Substrates that are normally repellant to certain types of inks or materials can also be used after altering surface energy characteristics by techniques such as plasma treatment. The melting point of the substrate is often a governing factor influencing the choice of substrate material, as the fabricated layer of material is heated to sintering temperatures along with the substrate. Commonly used substrates for fabricating test samples include glass, silicon wafers, ceramic disks, etc. which have very high melting temperatures. Substrates such as glass, silicon, etc. are sonicated in a bath of acetone and then thoroughly rinsed with iso-propyl alcohol to remove stains and loose particles embedded on the surface.

Layer/ film deposition

The sequence of steps involved in printing a layer of material via Aerosol Jet deposition are as follows:

1. Gas flow to the sheath is turned on. This process builds a pressure in the atomizing chamber due to the generation of a partial vacuum in the system.

2. Once the atomizing chamber is pressurized to a target pressure value (determined during nozzle calibration), gas flow to the atomizer is turned on.

3. The virtual impactor is also turned on by specifying the volume of gas to be removed from the atomizer exhaust. If the volumetric flow values of the atomizer, sheath and virtual impacting unit are represented as A, S and V, then the total volume of atomized gas flowing out through the nozzle is given by the expression, $N = (A - V) + S$.

4. The volumetric flows and the temperature controls are adjusted to produce the desired print line width, line thickness and mass flow.

5. Once the printing parameters have been established, the toolpath is loaded on to the device and executed. The toolpath can be repeated multiple times to build thickness of the deposited film.

Sintering

Sintering is the final step in the layer deposition/ fabrication process. It is done to improve the structural properties of the deposited layer, and also to remove sacrificial materials from the film that was deposited. The fabricated layer (along with the substrate) is sintered in a furnace at temperatures up to 1300°C. This thermal treatment cures the deposited layer and also burns off any organic substances present in the film. Alternatively, the laser system in the Optomec machine may also be used for localized sintering, as compared to co-sintering achieved through regular furnace based sintering.

Ideally, test samples are dried in air or in vacuum before sintering so as to reduce the residual stresses in the printed layer. Although the rate of heating (called ramp-up) can be reduced to as low as 1°C/min in the sintering furnace, it is sufficient to cause cracking in the films due to the thickness of the film and/or the surface chemistry of the substrate. Poor adhesion and cohesion properties between the substrate and the deposited film can also cause printed films to warp and detach from the substrate after sintering. A brief investigation on the cracking phenomenon observed in films printed via the Optomec Aerosol Jet deposition tool has been discussed in Section 3.3 of this work.

2.3 Process parameter modeling steps

Process parameter modeling was done using design of experiments in this work. Trial and error experiments were done during the initial phases of the experimentation to understand process capabilities and limitations. However, for accurately modeling the behavior of a response with respect to changes in process variables, a more scientific approach is required. Design of experiments was found to be a convenient technique to model parameters with the Optomec tool's process constraints. Process parameter studies found in literature [34, 35] revealed that steps involved in modeling are typically dictated by the process requirements and practical limitations. The sequence of steps followed for process parameter modeling in this thesis work was tailored for studying the Optomec tool as it was a relatively new prototype at the time this research was conducted. Figure 2.3 shows a general overview of the steps involved in modeling the process parameters in this work. These steps have been described briefly in the subsequent paragraphs and at length in Chapter 3.

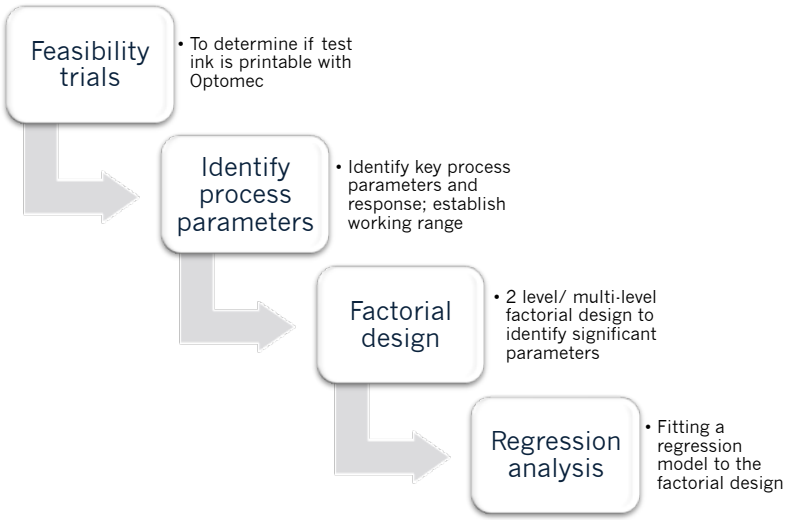

Figure 2.3: Steps involved in process parameter modeling

Initial feasibility trials were executed to determine the printability of the test ink with the Optomec tool. This was required as a novel test ink was used in the experiments (aqueous and ethylene glycol based nano-crystalline ceria) and their behavior in an atomizing environment had not been previously studied or recorded. This was followed by experiments to identify the key process parameters that influenced the thickness of the printed layer of material. Subsequent trial and error experiments were run to establish the limits of the process parameters under investigation. This helped create a workable design space in which the process parameters could be studied.

Screening of significant process parameters from the larger pool of process parameters was done with a simple 2 level full factorial experiment and a higher order (3 level) full factorial design. Regression models were generated after analysis of the factorial design and residuals. Validation runs were executed to check for curvature in the design space and estimate the accuracy of the regression equations generated from the screening experiment and the higher order design of experiments.

Chapter 3

Experimentation

3.1 Feasibility tests

The feasibility tests were conducted before the start of actual experimentation to determine of the test ink was printable with the Optomec tool. The test ink was a water based ink of nano sized crystalline cerium(IV) oxide (chemical formula CeO_2), also known as ceric oxide, cerium dioxide or just ceria and was provided by Cerion Energy, a nanoparticle production company based in Rochester, NY that manufactures nano scale CeO_2 for use as a diesel additive [36]. CeO_2 was chosen for the experimentation as it was a representative electrolyte material, easily available and manufactured under strict process control. The test solution had a solid loading fraction of about 2% by volume and an average particle size of about 8–10 nm. The size of particles (8–10 nm) in the ink and the ink viscosity (57 cP) were well within the suggested limits for the Optomec tool (1 μm or less for particle size and 1–1000 cP for viscosity).

The first set of experiments were designed to determine if the aqueous CeO_2 ink was printable using the Aerosol Jet process over a sustained period of time. A time based approach was taken to determine if the deposition was constant over time and to understand how flow rates influenced the print duration. This was required to determine the print size of the test samples for subsequent experiments in the investigation, as larger test samples would mean longer print duration.

A simple serpentine test tool path was designed using AutoCAD. To maintain printing during the desired deposition time, two approaches were considered: use a low translation speed of the print head for a long duration or use a higher translation speed with a longer toolpath. Reducing the translation speed of the print head resulted in non-uniform track widths during deposition. To overcome this problem, the track length from the original tool path was increased to generate serpentine patterns with increasing track lengths (refer Figure 3.1 and Table 3.1).

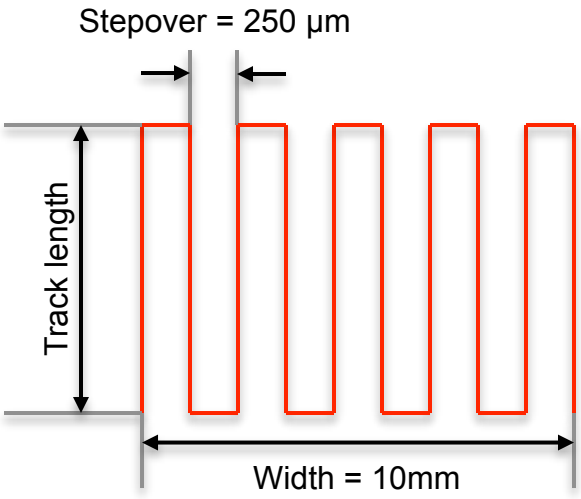

Figure 3.1: Parameters of the serpentine test tool path

Table 3.1: Tool path parameters for print feasibility tests

Trial	Track length (mm)	Stepover (µm)
1	10	250
2	20	250
3	40	250
4	80	250
5	160	250
6	250	250

The feasibility test runs were run at a constant translation velocity of 1mm/sec. Flow and temperature parameters were varied to determine the minimum value of flow rates at which deposition occurs. Based on trial and error experiments, process parameters for the deposition feasibility tests were found to be as shown in Table 3.2.

Table 3.2: Optomec tool parameters for deposition feasibility tests

Volumetric flows (ccm)			System temperatures (°C)		
Sheath	Virtual impactor	Atomizer	Platen	Tube	Atomizer
80	590	650	60	80	25

3.1.1 Maximum print duration

The deposition times for the trial runs with increasing track lengths are noted in Table 3.3. The Optomec tool was able to uniformly deposit thin lines of the test ink on two different substrates, viz. glass and mylar (polyethylene terephthalate) for up to approximately 3 hours without any noticeable defects during the deposition process.

Table 3.3: Print (deposition) duration for feasibility tests

Trial	Track length (mm)	Print time (minutes)
1	10	7.05
2	20	13.85
3	40	27.50
4	80	55.00
5	160	110.50
6	250	171.25

Flow rates on the atomizer and the the virtual impactor were increased such that their difference was constant (60cc) to determine the deposition cut off point. Test observations indicated that the higher flow rates in the atomizer and the virtual impactor lead to faster clogging in the deposition head.

At high flow rates, the amount of aerosolized droplets precipitating (or clogging) in the deposition head focusing cone increases multi-fold as compared with the clogging levels at reduced flow rates. Observations made on the deposition times as a function of flow rates (set values) are noted in Table 3.4. As can be seen from Figure 3.2, at flow rates of 2000 ccm in the atomizer, printing ceased in 3.5 minutes as compared to about 181 minutes at 800 ccm.

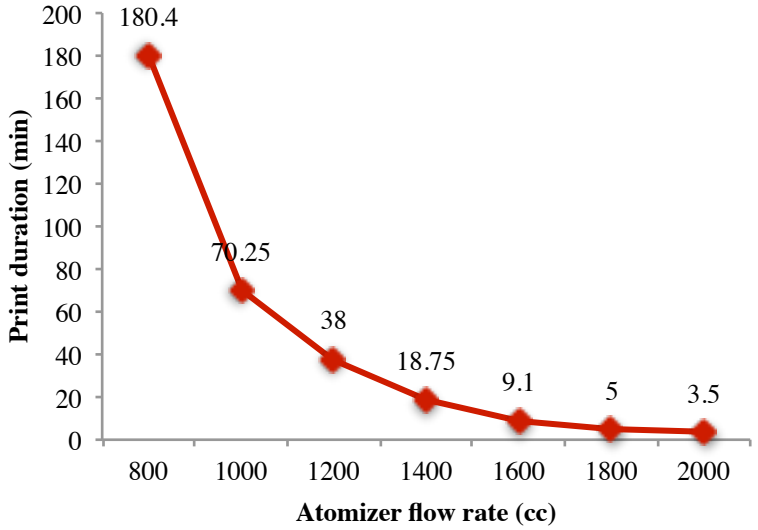

Figure 3.2: Print duration vs atomizer flow rate

Table 3.4: Print durations vs flow rates

Trial	Volumetric flow (ccm)			Print duration (minutes)
	Atomizer	Virtual impactor	Sheath	
1	2000	1940	80	3.50
2	1800	1740	80	5.00
3	1600	1540	80	9.10
4	1400	1340	80	18.75
5	1200	1140	80	38.00
6	1000	940	80	70.25
7	800	740	80	180.4

3.1.2 Electrolyte layer fabrication: trial prints

The feasibility trials and maximum print duration experiments helped identify the minimum and threshold flow rates for the aqueous CeO_2 ink. A new set of test samples were to be printed to determine parameters for fabricating a gas-tight layer of CeO_2, as this was a primary requirement of electrolyte layers in a SOFC. Figure 3.3 is a schematic representation of the orientation of the test squares on the wafers. The new samples were created as follows:

1. Ethylene glycol was added to the aqueous CeO_2 ink to help reduce the foaming phenomenon observed during the initial tests.

2. Each printed sample had a square geometry of 4mm x 4mm.

3. Six squares each were printed on two separate silicon wafers. Silicon wafers were chosen for better imaging of the samples during the Energy-dispersive X-ray (EDX) analysis. The build parameters for each of these test squares has been described in Table 3.5 and 3.6.

4. The first wafer was sintered at 350°C for five hours and the second wafer was sintered at 800°C for five hours.

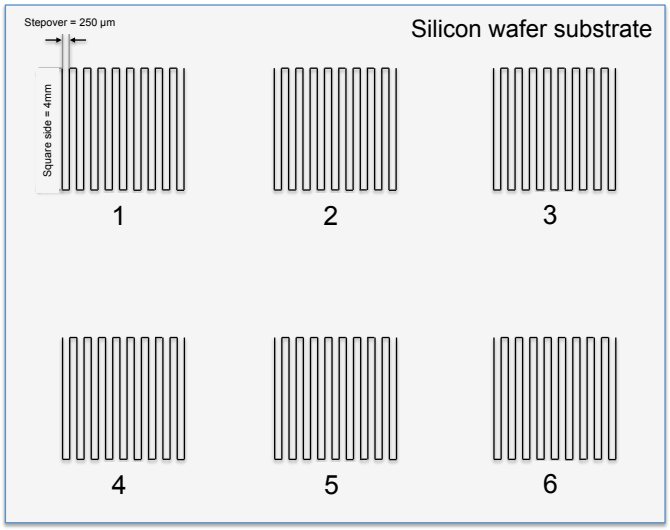

Figure 3.3: Schematic representation of orientation of test squares on silicon wafers

Table 3.5: Build parameters of test squares: wafer 1

Test square #	Square size (mm)	Line orientation (degrees)	Stepover (μm)	Number of layers
1	4	0	250	10
2	4	0	250	20
3	4	0	250	30
4	4	0	250	40
5	4	0	250	50
6	4	0	250	60

Table 3.6: Build parameters of test squares: wafer 2

Test square #	Square size (mm)	Line orientation (degrees)	Stepover (μm)	Number of layers
1	4	0	250	10
2	4	45	250	20
3	4	90	250	30
4	4	135	250	40
5	4	0	250	50
6	4	90	250	60

3.1.3 Post-sintering analysis

Post sintering, the two wafers were sent to Savannah River National Labs for EDX analysis. High resolution scan images and EDX spectrographs (Figures 3.4(a) to 3.7) of various samples in the two wafers indicated the presence of cerium (Ce), oxygen (O) and silicon (Si) on the test substrates. The micrographs also reveal nano sized particles of Ce (200-600 nm) on the substrate indicating that the deposited CeO_2 was in the crystalline form. Sintering did not seem to have impacted the structure of the Ce particles on the substrate insinuating since the nano Ce particles dispersed in the CeO_2 test ink were already in the crystalline form.

An inspection of the surface of the deposited layers in the high resolution images indicates several cracks (Figure 3.7). Since these cracks were non-existent immediately following deposition, it is surmised that they were the result of thermal stresses built up during the sintering process. The true purpose of sintering in Brinkman wt al.'s work [24] was to transform the amorphous ceria into crystalline ceria. Since this is not required with the CeO_2 test ink used in our experiments, it was decided to skip the sintering step altogether in the future experiments. The following is a summary of the results from the feasibility tests:

1. Aqueous CeO_2 ink was printable with the Optomec tool. Suitable process parameters for Aerosol Jet printing thin lines of ceria (100-220 µm) on silicon were determined.

2. Time studies for print durations indicated that the Optomec tool printed the CeO_2 ink for approximately 3 hours before deposition became unstable.

3. At higher volumetric flow rates in the atomizer, virtual impactor and sheath, higher rates of clogging and lower deposition times were observed. At maximum volumetric flow, deposition ceased after just 3.5 minutes.

4. Thin layers of crystalline ceria (10-20 µm) were successfully test printed successfully on a silicon substrate. EDX graphs of spots on the electrolyte layer indicated the presence of Ce, O and Si, suggesting intactness as well as cracks in the layer of ceria.

5. Ceria was deposited in crystalline form at the time of printing as opposed to amorphous form mentioned in Brinkman et al's work [24]. Post-deposition sintering builds stress in the crystalline ceria layer leading to cracks.

The water content of the ink used for printing the samples was identified as a significant factor in development of the cracks post-sintering due to its high vapor pressure. Ethylene glycol was chosen to replace water as the primary solvent in the ink due to its low vapor pressure and lower drying rate. Trials with an ethylene glycol based CeO_2 ink having 23% solid loading fraction were performed to determine the printability of this new ink formulation. The new ink (also supplied by Cerion Energy Ltd., Rochester) was prepared by shifting the CeO_2 in the aqueous ink to ethylene glycol by adding ethylene glycol to the aqueous solution and then slowly boiling the mixture to evaporate the water content.

Based on the feasibility tests and the scope of this work, five process parameters were identified as relevant to the thickness of a printed layer. They are:

1. Atomizer flow rate(ccm)
2. Difference in flow rate between atomizer and sheath, Δ (ccm)
3. Sheath flow rate (ccm)
4. Nozzle diameter (µm)
5. Platen translation speed (mm/sec)

Temperature controls in the Optomec tool were not considered because of several practical limitations concerning their use. Heating the atomizing cup caused the CeO_2 ink to break down and evaporate at an accelerated rate since it was water based. Tube temperatures less than 40°C resulted in a very lose flowing ink at the time of deposition while temperatures beyond 50°C caused the ink to dry out before reaching the deposition head leading to clogging issues in the system. Within the workable range of only about 10°C , there was no significant difference to print quality with changes to tube temperature. The platen heating was switched off to avoid the printed layers from 'wicking' into the print substrates, as porous die pressed SDC disks were to be used for experimentation in the future trials.

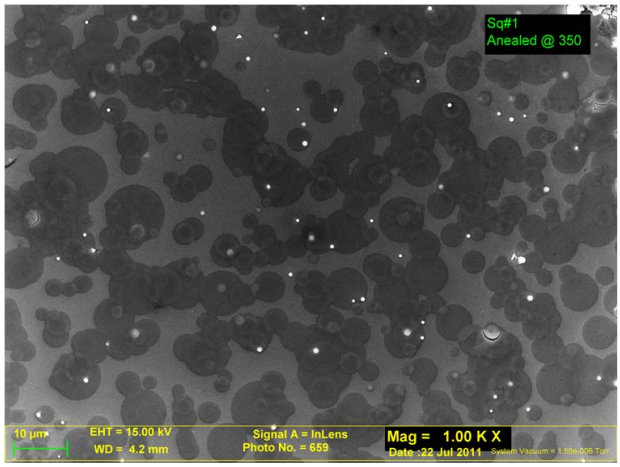

(a) 1KX magnification

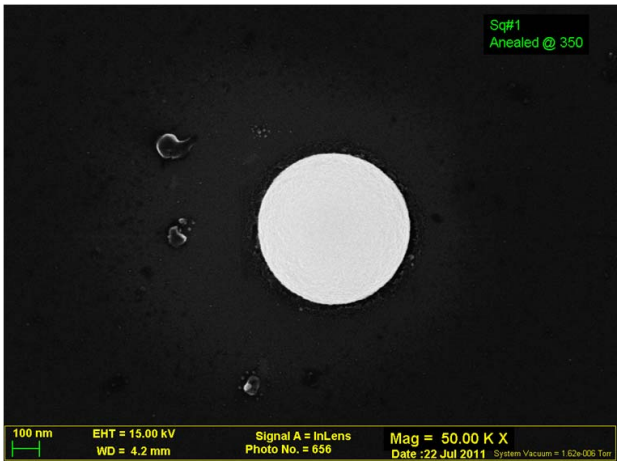

(b) 100KX magnification

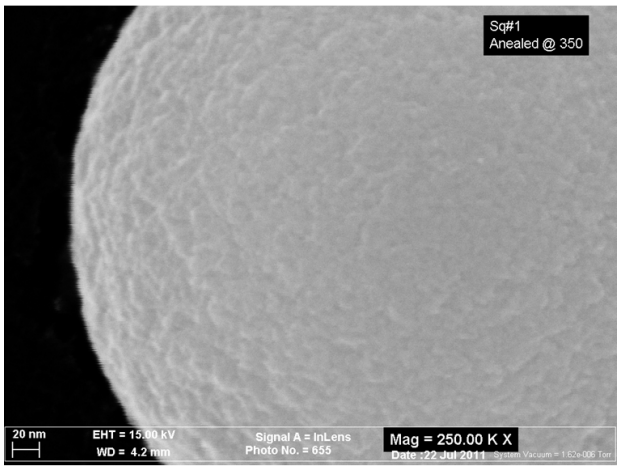

(c) 250KX magnification

Figure 3.4: SEM images of square 1 of wafer 1 (Sintered at 350°C)

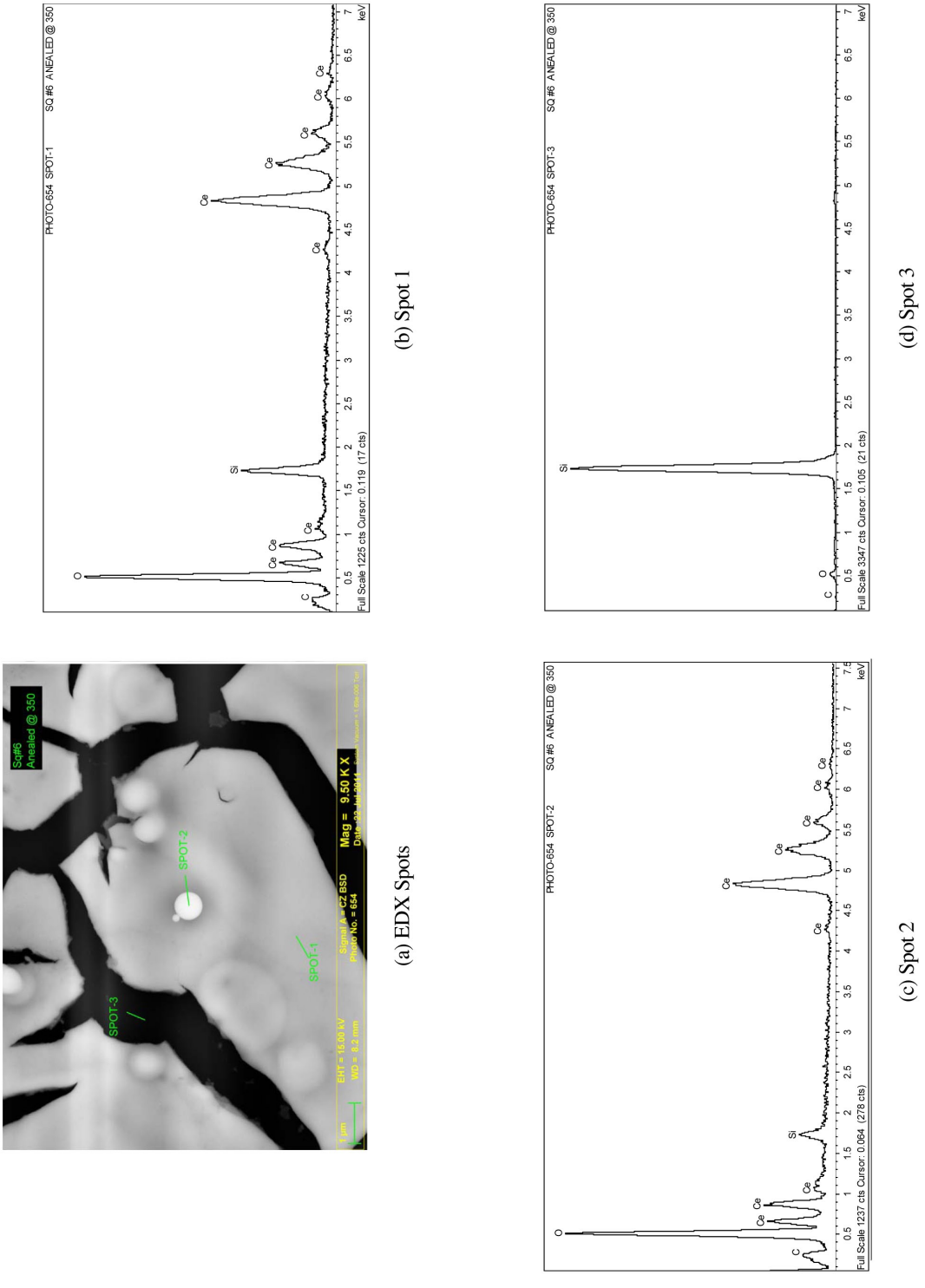

(a) EDX Spots

(b) Spot 1

(c) Spot 2

(d) Spot 3

Figure 3.5: X-ray spectroscopy of square 6 in wafer 1 (sintered at 350°C)

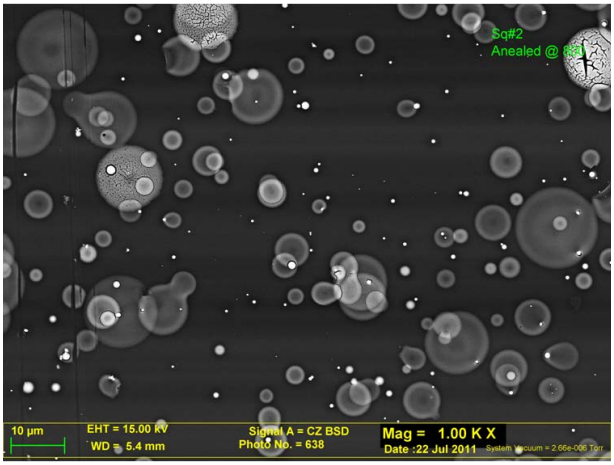

(a) 1KX magnification

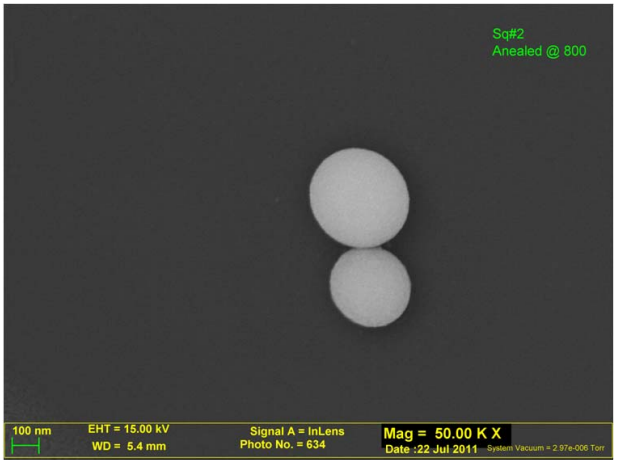

(b) 50KX magnification

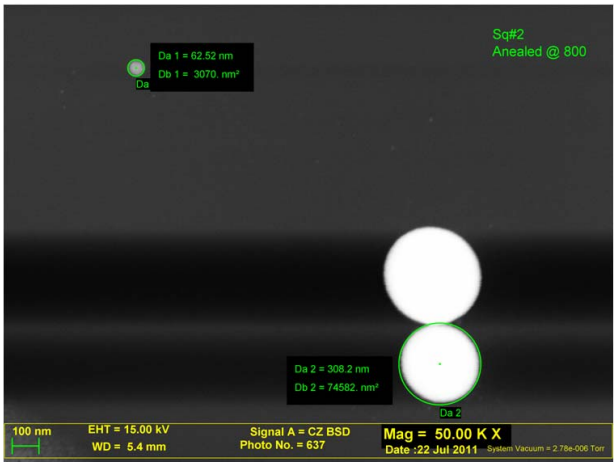

(c) 50KX magnification

Figure 3.6: SEM images of square 2 of wafer 2 (Sintered at 800°C)

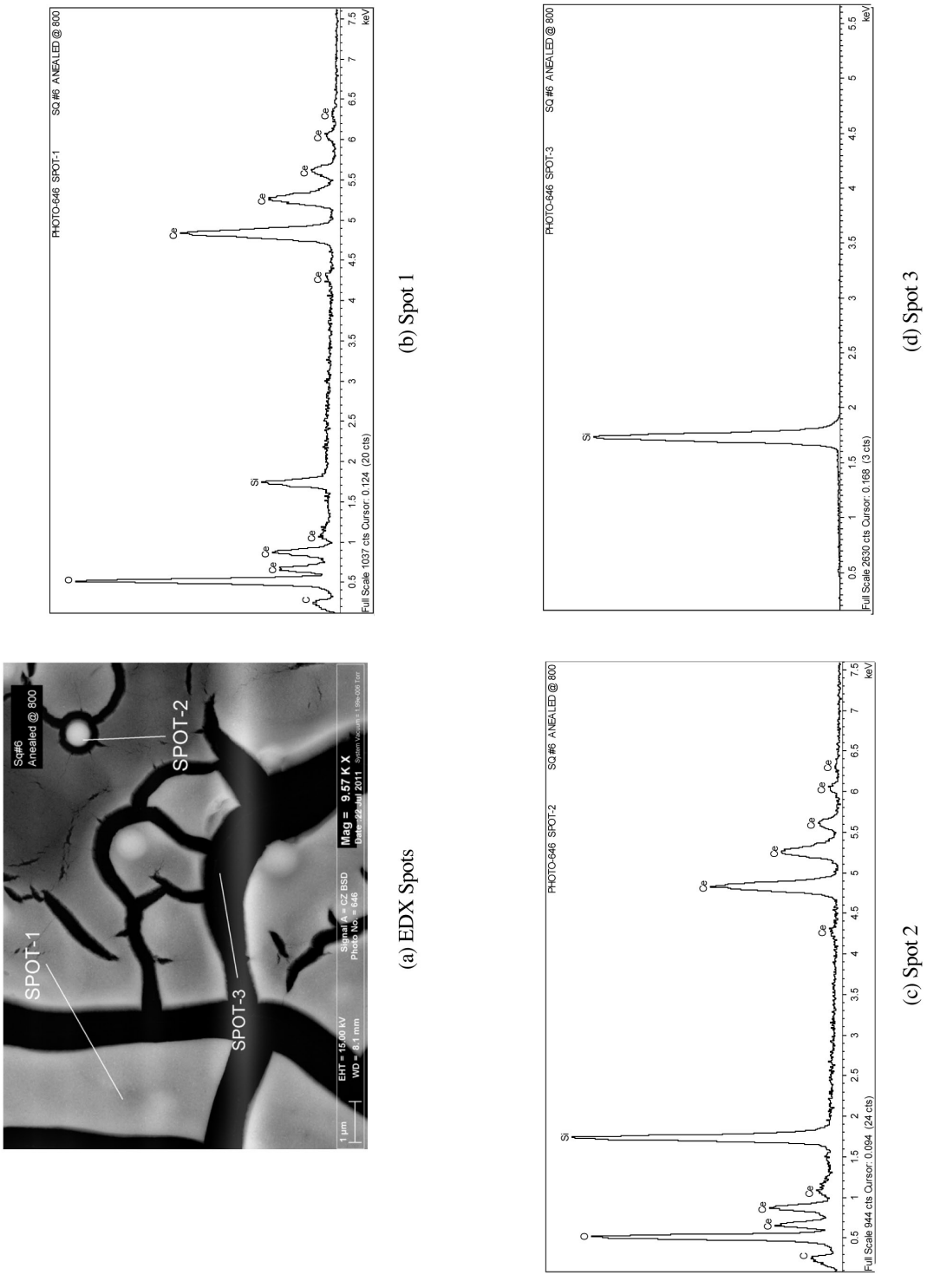

(a) EDX Spots

(b) Spot 1

(c) Spot 2

(d) Spot 3

Figure 3.7: X-ray spectroscopy of square 6 in wafer 2 (sintered at 800°C)

3.2 Process parameter modeling

3.2.1 Screening experiments

The design of experiments to model the process parameters was done in two phases viz., screening experiments followed by a higher order design. The screening experiments were done to identify the most significant process parameters with layer thickness as the response variable. A simple two level full-factorial design was created with five parameters using Minitab statistical software. The runs were executed in random order. A 4mm x 4mm square was the test pattern used for the screening trials, similar to the electrolyte fabrication trials. The levels used for screening (high and low) for the parameters under study were chosen based on previous trials to determine the minimum and maximum cut off points. High and low levels of the parameters and their coded names in Minitab software are tabulated in tables 3.7 and 3.8.

Table 3.7: Factor levels of test parameters

Level	Atomizer flow (ccm)	Δ (ccm)	Sheath flow (ccm)	Nozzle size (μm)	Platen speed (mm/sec)
High (+1)	1200	25	100	300	13
Low (-1)	800	5	25	150	5

Table 3.8: Coded Minitab names for test parameters

Process parameter	Coded Minitab name
Atomizer flow	A
Atomizer - VI flow (Δ)	B
Sheath flow	C
Nozzle size	D
Platen speed	E

The complete design of experiments (with randomized runs) for the screening trials from Minitab is as shown in Table 3.9. The experiments were performed at room temperature with die-pressed SDC disks as the substrate. A constant tube temperature of 40°C was maintained throughout the experiments and the platen was maintained at room temperature (i.e. no external heating). After printing, the printed samples were dried in air at room temperature for one hour followed by drying in an oven heated to 50°C for 2 hours before thickness measurements were recorded.

Table 3.9: Design of experiments for screening

Std Order	Run Order	A	B	C	D	E	Response
29	1	-1	-1	1	1	1	6.00
1	2	-1	-1	-1	-1	-1	10.75
28	3	1	1	-1	1	1	24.25
22	4	1	-1	1	-1	1	1.75
31	5	-1	1	1	1	1	7.25
14	6	1	-1	1	1	-1	7.75
9	7	-1	-1	-1	1	-1	19.50
3	8	-1	1	-1	-1	-1	8.50
15	9	-1	1	1	1	-1	13.75
25	10	-1	-1	-1	1	1	4.75
16	11	1	1	1	1	-1	13.50
13	12	-1	-1	1	1	-1	8.50
23	13	-1	1	1	-1	1	3.75
29	14	-1	1	-1	-1	1	5.75
11	15	-1	1	-1	1	-1	14.00
20	16	1	1	-1	-1	1	12.25
8	17	1	1	1	-1	-1	9.75
30	18	1	-1	1	1	1	5.50
24	19	1	1	1	-1	1	4.00
27	20	-1	1	-1	1	1	9.00
18	21	1	-1	-1	-1	1	4.50
7	22	-1	1	1	-1	-1	9.75
21	23	-1	-1	1	-1	1	3.75
4	24	1	1	-1	-1	-1	6.25
5	25	-1	-1	1	-1	-1	3.50
32	26	1	1	1	1	1	9.75
10	27	1	-1	-1	1	-1	12.00
6	28	1	-1	1	-1	-1	3.75
2	29	1	-1	-1	-1	-1	5.00
17	30	-1	-1	-1	-1	1	3.25
26	31	1	-1	-1	1	1	8.75
12	32	1	1	-1	1	-1	12.00

The thickness of the printed 4mm x 4mm square was measured using two distinct methods (equipment). The first method used high resolution microscopy with a Hirox KH-7700 digital microscope.The substrates were mounted on the microscope platform, and a small portion of each test square was brought under focus at very high resolution (2000x and higher). To measure the printed layer thickness, the substrate (assumed to be the base level of the printed layer) and the top surface of the printed layer were separately brought into focus. The microscope's software is able to determine the thickness of the printed layer by measuring the focal plane height of the top and bottom images and then taking the difference between the two numbers.

The second method for measuring thickness employed a laser profilometer. The Keyence (model IL-030) laser profilometer used for this study was a non-contact profilometer with a resolution of 1 μm. The profilometer has a sensor head, an amplifier unit and a communication unit. The sensor head produces a laser beam, the amplifier unit amplifies the analog output and the communication unit transmits the output to the computer via a serial port. Thickness is measured by finding a flat portion of the substrate (assumed to be the base of the printed layer) and then slowly moving the substrate until the laser is focused on the top surface of the printed sample. The beam is reflected off the sampled surface of the printed layer back into a receiver unit that computes the thickness, and this information is passed on to the amplifier [37]. The printed samples were mounted onto computer controlled X-Y stage, and the laser profilometer's output was collected in an Excel spreadsheet. Thicknesses measured by these two devices were almost similar with a maximum difference of about 0.75 μm (see Table 3.10).

A plot of the thickness measurements taken by the Hirox microscope KH-7700 and the laser profilometer (IL-030) is shown in Figure 3.8. As can be seen from Figure 3.8, the fitted linear trendline for the microscope vs profilometer readings has a slope close to 1, indicating that the thickness measurements between the two methods are in close agreement. This was also observed from the plot of the difference in thickness measurements whose trendline slope is close to 0. The thickness measurements made with the Keyence laser profilometer for the screening experiments (in μm) are noted in the response column in Table 3.9.

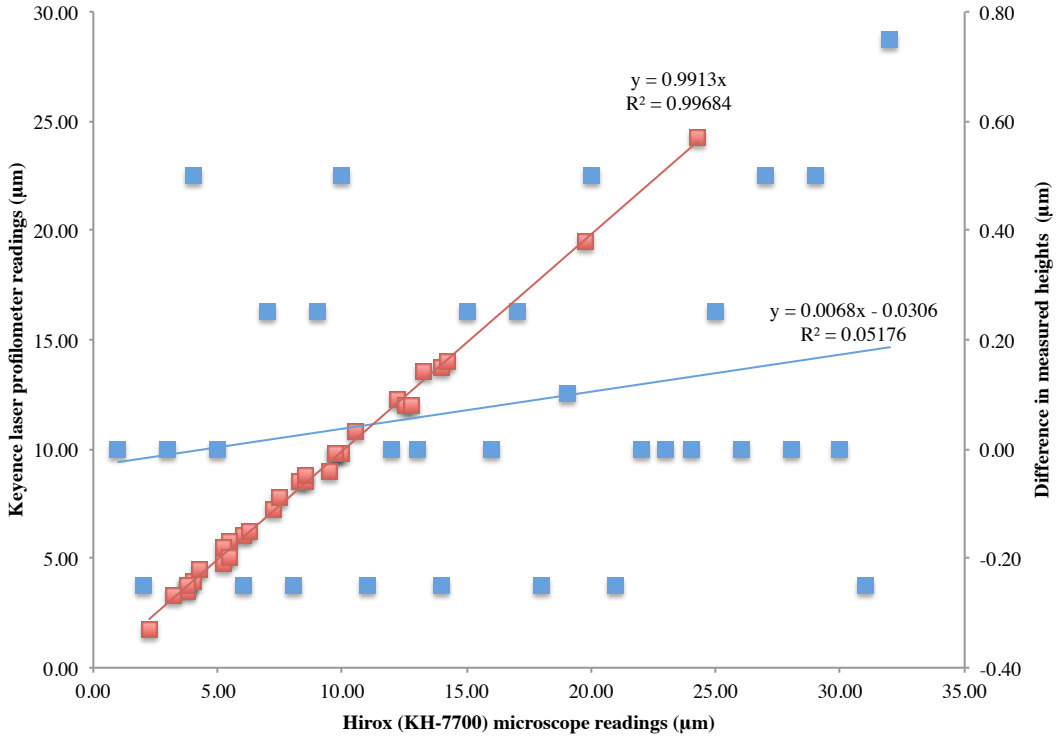

Figure 3.8: Comparison of thicknesses measured via Hirox microscope and Keyence profilometer

Most statistical tests are based on the assumption that the residuals of the sampled data is normally distributed to constrain the limit of variability [38]. Hence a distribution identification test on the residuals of the response (layer thickness) was run in Minitab to check if the residual data followed normal distribution. Acceptable p-values for the distribution identification test was 0.05 and greater (assuming an α level of 5%). The results (see Figure B.1 in Appendix B) indicated that the residuals were not normally distributed (p-value < 0.05).

Mathematical transformations such as square root transform, exponential transform, lognormal transform, etc. are commonly used to transform data such that their residuals are transformed from non-normal distributions to normally distributed data [39]. A square root transformation on the response variable (layer thickness) increased the p-value of the residuals data in the distribution identification test to 0.721 (Figure B.2 in Appendix B) in a distribution identification test. Although a few other transformations may have

Table 3.10: Comparison of measured thicknesses

StdOrder	Run Order	Film thickness (µm)		Difference (µm)
		Hirox	Keyence	
29	1	6.00	6.00	0.00
1	2	10.50	10.75	-0.25
28	3	24.25	24.25	0.00
22	4	2.25	1.75	0.50
31	5	7.25	7.25	0.00
14	6	7.50	7.75	-0.25
9	7	19.75	19.50	0.25
3	8	8.25	8.50	-0.25
15	9	14.00	13.75	0.25
25	10	5.25	4.75	0.50
16	11	13.25	13.50	-0.25
13	12	8.50	8.50	0.00
23	13	3.75	3.75	0.00
19	14	5.50	5.75	-0.25
11	15	14.25	14.00	0.25
20	16	12.25	12.25	0.00
8	17	10.00	9.75	0.25
30	18	5.25	5.50	-0.25
24	19	4.00	3.90	0.10
27	20	9.50	9.00	0.50
18	21	4.25	4.50	-0.25
7	22	9.75	9.75	0.00
21	23	3.75	3.75	0.00
4	24	6.25	6.25	0.00
5	25	3.75	3.50	0.25
32	26	9.75	9.75	0.00
10	27	12.50	12.00	0.50
6	28	3.75	3.75	0.00
2	29	5.50	5.00	0.50
17	30	3.25	3.25	0.00
26	31	8.50	8.75	-0.25
12	32	12.75	12.00	0.75

returned acceptable p-values in the distribution identification test, they were not chosen to transform the data as the square root transform was mathematically simpler in comparison to the other transforms.

The factorial design with the response variable set to the square root of the layer thickness was analyzed using the factorial analysis module in Minitab. A half normal plot of effects (with α value set to 0.05) was generated with factors up to order 5 (Figure 3.9). Since interactions between higher order terms (order 3 and above) were statistically very unlikely to be significant, the half normal plot was regenerated to include

only up to second order interactions (Figure 3.10). Significant parameters were arrived at based on visually estimating the line of best fit to the half normal plot and not the blue significance line generated by Minitab. Significant process parameters from Figure 3.10 were observed to be parameters B (Δ), D (nozzle size) and E (platen velocity). Interaction effect AE was not included as part of the reduced model as it was a higher order effect. Parameter C (sheath) was excluded from the reduced model as lower sheath levels caused deposited films to swell post-deposition and this caused problems with height measurements.

An analysis of residuals from the reduced model with just the significant factors B, D and E obtained from Minitab (Figure B.3 in Appendix B) is discussed here. The normal probability plot of the residuals had no major deviations indicating that the residuals were more or less normally distributed. Lack of observable patterns in the versus fits plot suggested that the mean of the error terms was approaching zero. A non-trending versus order plot was indicative of well spread deviations due to uncontrollable factors (effect of randomizing the run order). We proceed to fitting a regression equation to the reduced parameter model in Minitab. The regression equation (see Section B.3 in Appendix B) obtained from Minitab (significant to 2 digits) is,

$$\mathrm{Sqrt(Height)} = 2.8067 + 0.305632\ \mathrm{Delta} + 0.433245\ \mathrm{Nozzle} - 0.265175\ \mathrm{Platen\ velocity} \tag{3.1}$$

The 'Summary of Model' output generated from the regression analysis in Minitab is summarized as follows: S = 0.569211, R-Sq = 55.35%, R-Sq(adj) = 50.57%. The output statistic S is the measured standard error in the model and is 0.569211. Since the analyzed response was the square root of layer thickness, the standard error is actually $(0.569211)^2$ µm. The predicted square root of residuals (R-Sq) was about 55% indicating that the regression model only accounts for 55% of the deviation observed in the recorded data points. This led to the design of a higher order experiment to obtain a better fitting regression model (discussed in Section 3.2.3).

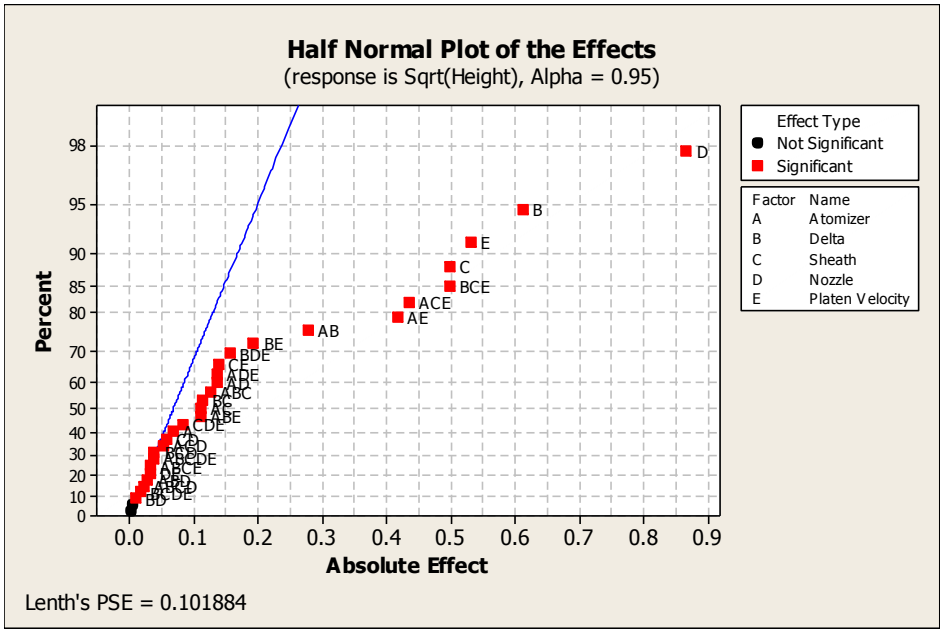

Figure 3.9: Factorial analysis: half normal plot of effects

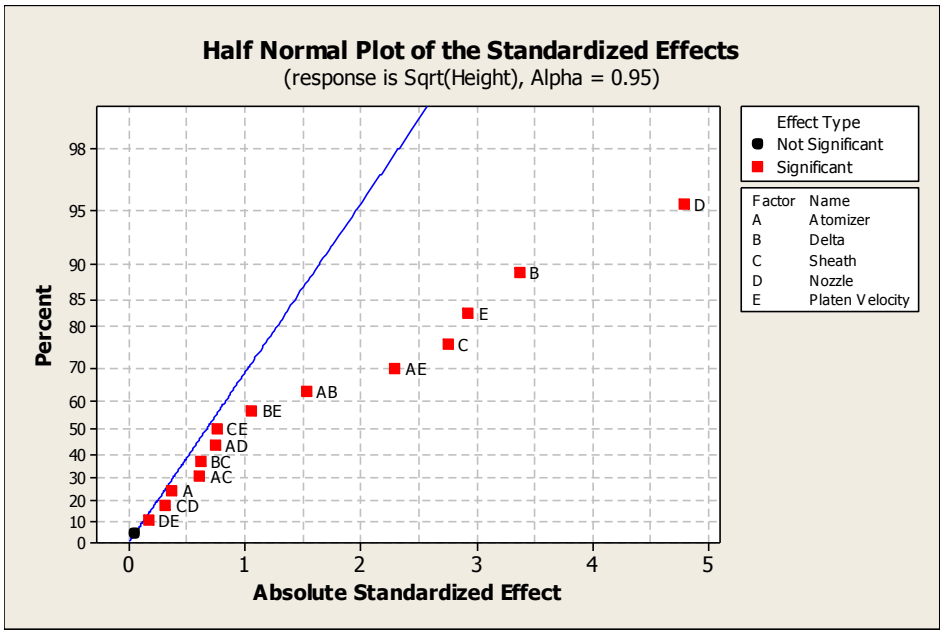

Figure 3.10: Factorial analysis: half normal plot of effects (upto second order)

3.2.2 Verification runs

Using equation 3.1 as a baseline, a series of experiments with factor levels intermediate to the high and low levels chosen for the screening experiments (see Table 3.7 in section 3.2) were designed as verification runs for the screening experiments. The levels and the design of experiments for the verification runs are as shown in table 3.11. Encoded values for each of the parameters in the verification runs were calculated using the method below [40].

$$a_c = \frac{a_{uc} - \bar{a}}{\hat{a}} \tag{3.2}$$

where,

a_c is the coded value of parameter a

a_{uc} is the real value of parameter a

$\bar{a}$ = (a_{max} + a_{min})/2

$\hat{a}$ = (a_{max} - a_{min})/2

a_{max} = maximum value of parameter a (set for screening trials)

a_{min} = minimum value of parameter a (set for screening trials)

Table 3.11: Parameter levels for verification experiments

Parameter	Level 1		Level 2		Level 3	
	Actual	Encoded	Actual	Encoded	Actual	Encoded
Delta (Δ)	10 ccm	-0.5	15 ccm	0	20 ccm	0.5
Nozzle size	150 µm	-1	-	-	250 µm	1
Platen velocity	7 mm/sec	-0.5	9 mm/sec	0	11 mm/sec	0.5

The verification experiments were run with a constant atomizer flow setting of 1200 ccm and sheath flow of 100 ccm. The samples were again printed on to die pressed SDC disks. The tube temperature was maintained at 40°C, and the platen was maintained at room temperature. The samples were air-dried at room temperature for 1 hour followed by drying in an oven for 2 hours at 50°C. The thickness was measured using the Keyence laser profilometer equipment. Thickness measurements for the verification runs are noted in Table 3.12.

Table 3.12: Screening verification: predicted vs actual thickness using screening regression equation

Run Order	Delta (ccm)	Nozzle size (μm)	Platen velocity (mm/sec)	Actual thickness (μm)	Predicted thickness (μm)	Difference μm	Difference %
1	20	250	7	12.25	12.43	0.18	1.45%
2	15	250	7	10.75	11.37	0.62	5.80%
3	10	250	7	10.5	10.37	-0.13	-1.27%
4	20	250	11	10.5	10.63	0.13	1.23%
5	20	250	9	11.25	11.51	0.26	2.32%
6	10	250	9	9.75	9.53	-0.22	-2.25%
7	15	250	11	9.25	9.66	0.41	4.39%
8	10	250	11	8.75	8.73	-0.02	-0.24%
9	15	250	9	10.25	10.50	0.25	2.41%
10	20	150	7	7.25	7.07	-0.18	-2.49%
11	15	150	7	6.25	6.28	0.03	0.48%
12	10	150	7	5.5	5.54	0.04	0.68%
13	20	150	11	5.75	5.73	-0.02	-0.35%
14	20	150	9	6.25	6.38	0.13	2.11%
15	10	150	9	5	4.93	-0.07	-1.38%
16	15	150	11	5.25	5.02	-0.23	-4.35%
17	10	150	11	4.25	4.36	0.11	2.59%
18	15	150	9	5.75	5.63	-0.12	-2.03%

The thicknesses measured from the verification runs were compared with the predicted thickness values calculated from equation 3.1. On average, the deviation of the actual thickness values was $\pm 2.58\%$ from the mean. The predicted and actual thickness values and the measured deviation have also been recorded in Table 3.12. 99% of observed variations in the predicted values fall within the standard error limits predicted for the existing regression model, mean $\pm(0.569211)^2$ μm from Section B.3 of Appendix B.

A single center point run was also executed with three replications to check for curvature within the end planes of the design cube. The factor levels for the significant parameters were: Delta (Δ) = 15 ccm, nozzle size = 200 µm and platen velocity = 9 mm/sec. These correspond to coded values of 0 for the three parameters (from Table 3.11). The predicted and actual responses for these runs and the percentage error in the prediction model are noted in Table 3.13. The average percentage deviation of the actual response from the predicted values from the regression model calculated for all the verification runs, including the center point runs was $\pm 2.45\%$.

Table 3.13: Center point runs - predicted vs actual thickness using screening regression equation

Replicate	Actual thickness (µm)	Predicted thickness (µm)	Difference (%)
1	7.75	7.82	1.62%
2	8.00	7.82	-1.55%
3	7.75	7.82	1.62%

3.2.3 Higher order design

Since the verification runs for the regression model fitted to the screening experiments were in good agreement with the predicted response values and were within the limits of the standard error, there was no evidence to support curvature in the fitted regression equation. Though there is a possibility of the existence of curvature outside the current design space, it can be argued that some of the process parameters become obsolete while others cannot be tested outside the design space due to practical limitations of the equipment. However, to establish lack of curvature inside the design space, a three level design with factor levels set at mid-points of the design cube was created. The parameter levels and the design of experiments for the higher order design is noted in tables 3.14 and 3.15. The atomizer flow rate was maintained at 1200 ccm and the sheath was maintained at 100 ccm through the course of the verifications runs. As before, the samples were printed onto a die pressed disc of SDC with a tube temperature of 40°C while the platen was maintained at room temperature. To reduce setup times associated with cleaning at higher flow rates and to maximize utilization of the die pressed SDC disks as substrates, 1mm x 1mm squares were printed instead of 4mm x 4mm squares.

The printed samples were air-dried for 1 hour followed by oven drying at 50°C for 2 hours. The thickness (response) of the test samples was measured using the Keyence laser profilometer. The measured layer thickness values from the higher order design have been note in Table 3.15.

Table 3.14: Parameter levels for higher order design runs

Parameters	Minitab coded name	Levels		
		Low (-1)	Midpoint (0)	High (+1)
Delta (ccm)	B	5	15	25
Nozzle Size (μm)	D	150	200	250
Platen velocity (mm/sec)	E	5	9	13

Table 3.15: Higher order design of experiments and response

StdOrder	Run Order	B	D	E	Response
21	1	1	-1	1	6.00
11	2	0	-1	0	5.75
12	3	0	-1	1	4.75
14	4	0	0	0	7.75
8	5	-1	1	0	8.50
27	6	1	1	1	10.75
25	7	1	1	-1	14.50
5	8	-1	0	0	6.50
16	9	0	1	-1	12.25
22	10	1	0	-1	11.25
15	11	0	0	1	6.50
23	12	1	0	0	9.75
9	13	-1	1	1	7.25
1	14	-1	-1	-1	5.50
3	15	-1	-1	1	3.50
17	16	0	1	0	10.75
26	17	1	1	0	12.50
10	18	0	-1	-1	7.00
13	19	0	0	-1	9.50
19	20	1	-1	-1	8.75
7	21	-1	1	-1	10.75
24	22	1	0	1	8.25
4	23	-1	0	-1	7.75
20	24	1	-1	0	7.25
6	25	-1	0	1	5.25
2	26	-1	-1	0	4.25
18	27	0	1	1	8.75

To better the accuracy of the process parameter model, regression analysis was done on the higher order design. Section B.4 of Appendix B shows the Minitab outputs for the regression analysis done on the higher order design. The updated regression equation (significant to 2 digits) obtained from Minitab is,

$$\text{Sqrt(Height)} = 2.82534 + 0.290751\ \text{Delta} + 0.424714\ \text{Nozzle} - 0.256312\ \text{Platen velocity} \tag{3.3}$$

The 'Summary of Model' output for the regression analysis of the higher order design of experiment from Minitab reveals a significant improvement to the S statistic as well as the R-Sq values. The standard error (S statistic) is now 0.0294616 and the R-Sq value is a high 99.67%. The following inferences were arrived at after a comparison of the data from screening and the higher order design of experiments.

1. There is consistency in the data sets. Both the screening and the higher order experiments were executed with the same high and low levels for significant parameters. In the higher order experiments, the center point was included as an intermediate level. The measured responses from both these experiment sets fall within the same range with a very minor percentage of deviation.

2. The standard error in the higher order experiments (0.0294616) was reduced significantly as compared to the error of the screening experiments (0.569211). This reduction in the spread of deviation had a few attributable causes. They are as follows:

   (a) The size of the printed test sample in the higher order experiments was 1mm x 1mm as compared to 4mm x 4mm in the screening experiments. This represents a print duration shortened by about 93.5% for the higher order design test prints (326 seconds for a 4mm x 4mm square as opposed to 21 seconds for a 1mm x 1mm square). Because the chances of overspray improve significantly with increase in print duration with the Optomec tool, the likelihood of increased deviations in thickness measurements due to the size of the test samples in the screening experiments can be entertained.

   (b) Thickness measurements were taken with the Keyence laser profilometer by sampling the test squares over the surface. The presence of cracks (microscopic and macroscopic) can add variability to the measured thicknesses causing an increase in deviation in the screening experiments.

Re-calculating the predicted thicknesses for the screening verification runs it was seen that the percentage deviation between the predicted and actual values had reduced to 2.42% (calculated from Table 3.16). This number further drops to 2.30% with the inclusion of center points (calculated from Table 3.17) to the sample set. It can hence be said that the updated regression equation improved the resolution of the experiment and validated the results from the screening experiment in a more statistically significant manner, as the R-Sq values increased to 99.67% in the higher order design as compared to 55.35% from the screening experiments.

Table 3.16: Verification runs: predicted vs actual thickness using updated regression equation

Run Order	Actual thickness (µm)	Predicted thickness (µm)	Difference	
			(µm)	(%)
1	12.25	12.42	-0.17	1.35%
2	10.75	11.41	-0.66	6.16%
3	10.50	10.45	0.05	-0.46%
4	10.50	10.68	-0.18	1.67%
5	11.25	11.53	-0.28	2.48%
6	9.75	9.64	0.11	-1.14%
7	9.25	9.75	-0.50	5.36%
8	8.75	8.86	-0.11	1.25%
9	10.25	10.56	-0.31	3.05%
10	7.25	7.15	0.10	-1.36%
11	6.25	6.39	-0.14	2.32%
12	5.50	5.68	-0.18	3.28%
13	5.75	5.85	-0.10	1.67%
14	6.25	6.48	-0.23	3.71%
15	5.00	5.09	-0.09	1.72%
16	5.25	5.16	0.09	-1.64%
17	4.25	4.52	-0.27	6.46%
18	5.75	5.76	-0.01	0.23%
19	7.75	7.98	-0.23	2.91%
20	8.00	7.98	0.02	-0.22%
21	7.75	7.98	-0.23	2.91%

Table 3.17: Center point runs: predicted vs actual thickness using updated regression equation

Replicate #	Actual thickness (µm)	Predicted thickness (µm)	Difference (%)
1	8.00	7.98	-0.22%
2	7.75	7.98	2.91%
3	7.75	7.98	2.91%

3.3 Drying methods

Factors such as drying methods, curing temperatures, ink chemistry, etc. external to the Optomec Aerosol Jet deposition system had a noticeable impact on the thickness as well as the surface quality of the printed electrolyte layer. A brief investigation on drying methods is presented in this section.

3.3.1 Air drying

Drying is one of the most significant external parameters impacting the thickness of the printed electrolyte layer as it immediately follows the deposition process. Since the electrolyte layer was fabricated with an ethylene glycol based ink, there exists a high probability that some portions of the printed layer were in the liquid phase. Additionally, complete evaporation of ethylene glycol from the ink at the time of deposition is not possible since the heat applied to the tube heater is only 40°C while the boiling point of ethylene glycol is 197.1°C [41]. Also, it is unclear as to how the thickness of the printed electrolyte will vary in response to the ethylene glycol evaporation.

Initial experiments were conducted with 4mm x 4mm test squares printed in aluminum weigh cups. The weights of the printed ink samples were measured using a AND-HR60 high resolution analytical balance. Ten test squares from the screening DOE were printed with process parameter values set to high for all five parameters (Tables 3.9 and 3.7). The tube heater was maintained at 40°C and the platen maintained at room temperature. Five passes were run for each test square (as opposed to one pass throughout Section 3.2) due to the least count limitation on the weighing scale. The measured weights represent the combined weights of the solid and the liquid phase in the printed electrolyte ink and have been noted in column 2 of Table 3.18. The printed test samples were dried in air with no external heating or pressure. The weight of the test specimens were noted at time intervals of 1, 2, 4, 8, 12 and 24 hours respectively. Columns 3 to 8 of table 3.18 tabulates the measured weights of the test samples at the specified time intervals; column 9 notes the loss in weight in the test samples as a percentage of the original weight. The data indicates that much of the loss in weight in the printed samples occurs during the first 4 hours after printing beyond which it is more or less stable.

Table 3.19 tabulates the measured thicknesses at the start and end of the experiments as hourly readings were impractical. As can be seen from Tables 3.18 and 3.19, the printed samples lost an average of 28% in weight and 30% in thickness from start to finish. However, cracks (micro and macro scale) developed on almost all test specimens after the 2 hour mark (figures 3.11 and 3.12).

Table 3.18: Air drying: weight loss over time

Test sample #	Starting weight (g)	Weight of sample (g) after time elapsed (hours)						Weight loss (%)
		1	2	4	8	12	24	
1	0.0015	0.0013	0.0013	0.0012	0.0012	0.0012	0.0011	26.67
2	0.0018	0.0016	0.0015	0.0015	0.0014	0.0013	0.0013	27.78
3	0.0015	0.0014	0.0013	0.0013	0.0012	0.0011	0.0011	26.67
4	0.0017	0.0015	0.0015	0.0014	0.0014	0.0013	0.0012	29.41
5	0.0018	0.0016	0.0014	0.0014	0.0014	0.0014	0.0013	27.78
6	0.0016	0.0015	0.0015	0.0014	0.0013	0.0013	0.0011	31.25
7	0.0015	0.0014	0.0013	0.0013	0.0012	0.0011	0.0011	26.67
8	0.0017	0.0015	0.0015	0.0014	0.0013	0.0012	0.0012	29.41
9	0.0016	0.0016	0.0015	0.0014	0.0013	0.0012	0.0011	31.25
10	0.0017	0.0016	0.0016	0.0015	0.0014	0.0013	0.0012	29.41

Table 3.19: Air drying: reduction in film thickness over time

Test sample #	Starting thickness (µm)	Ending thickness (µm)	% difference
1	13.00	9.25	28.85%
2	15.50	11.25	27.42%
3	12.75	9.25	27.45%
4	14.75	10.00	32.20%
5	15.50	10.75	30.65%
6	14.00	9.25	33.93%
7	13.00	9.00	30.77%
8	14.75	10.25	30.51%
9	14.25	9.50	33.33%
10	15.00	10.50	30.00%

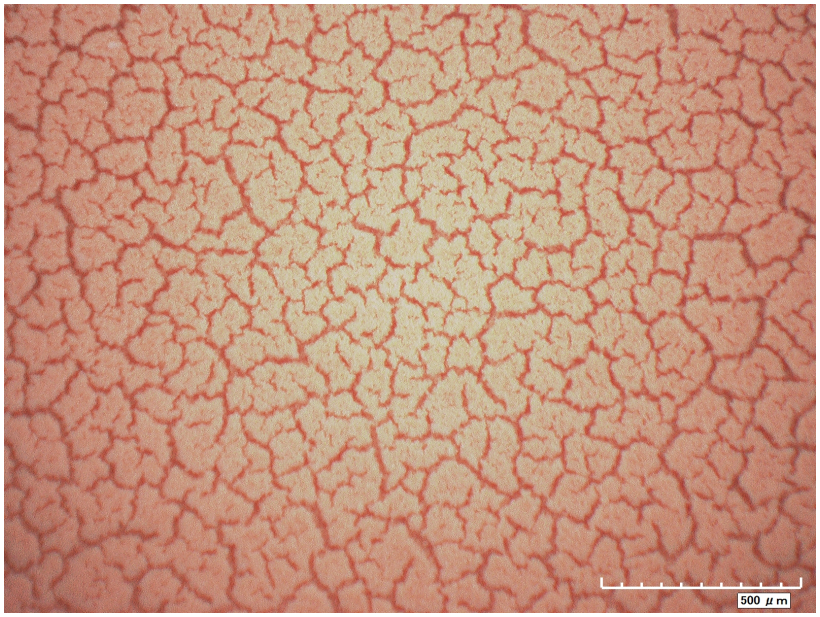

Figure 3.11: Micro cracking in air dried sample 2 hours after deposition

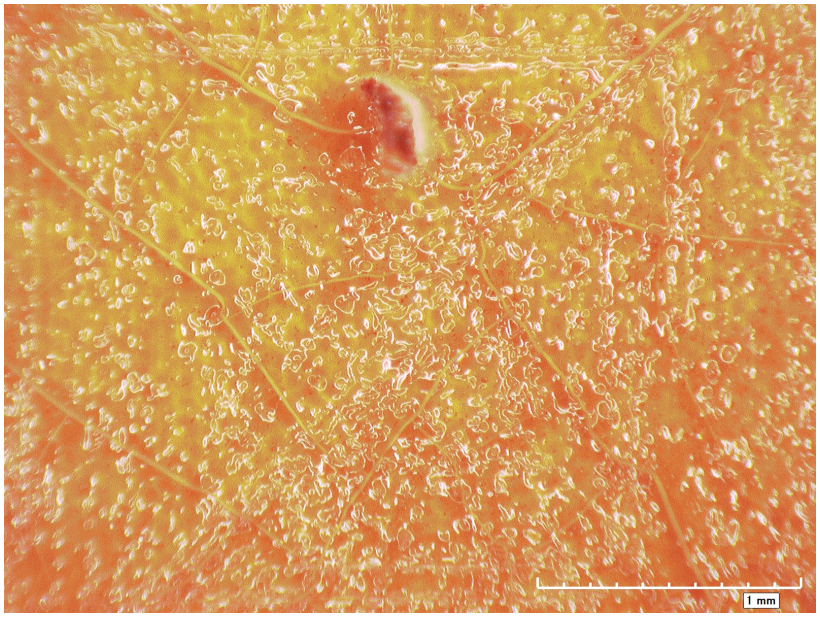

Figure 3.12: Macro cracking in air dried sample 2 hours after deposition

3.3.2 Heat assisted drying

A second set of experiments (repeat of the same experiments just described) was executed to investigate whether or not the application of heat expedited the weight loss phenomenon as well as the cracking. The test samples were printed in aluminum weigh cups. The weight and thickness of the printed material was immediately measured, and the samples were then quickly transferred to an oven maintained at 50°C. All samples were maintained in the oven for 4 hours and the weights were measured at one hour intervals. The final film thickness was noted after all specimens were removed from the oven. As expected, the weight loss was highest in the first hour and stabilized after three hours. The change in weight and thickness (in terms of % loss) was slightly higher in this case, with measured value decreasing by an average of 40% for thickness and 39% for weight. Table 3.20 tabulates the weights and thicknesses of the test specimen. While the test samples reached steady weight and thickness more quickly compared with the air drying process, as expected, cracking was still widely observed across the samples. Higher drying temperatures (100°C and above) compounded the cracking phenomenon as the deposited films started to peel away from the printed substrate (Figure 3.13). A similar effect was observed on samples printed on die pressed SDC disks as well.

Table 3.20: Heat assisted drying: reduction in thickness and weight

Trial #	Thickness (μm)		% diff	Starting	Weight (g) after elapsed time (hours)				% diff
	Starting	Ending		weight (g)	1	2	3	4	
1	14.75	8.00	45.76%	0.0017	0.0012	0.0011	0.0010	0.0010	41.18%
2	13.75	8.25	40.00%	0.0016	0.0012	0.0011	0.0010	0.0010	37.50%
3	16.50	9.75	40.91%	0.0019	0.0013	0.0012	0.0011	0.0011	42.11%
4	15.75	9.25	41.27%	0.0018	0.0013	0.0012	0.0012	0.0011	38.89%
5	13.75	9.25	32.73%	0.0016	0.0013	0.0012	0.0011	0.0011	31.25%
6	14.75	8.25	44.07%	0.0017	0.0011	0.0010	0.0010	0.0010	41.18%
7	16.00	9.75	39.06%	0.0018	0.0013	0.0013	0.0012	0.0012	33.33%
8	13.00	7.00	46.15%	0.0015	0.0010	0.0009	0.0009	0.0008	46.67%
9	14.75	8.50	42.37%	0.0017	0.0011	0.0011	0.0011	0.0010	41.18%
10	14.75	9.25	37.29%	0.0017	0.0013	0.0012	0.0012	0.0011	35.29%

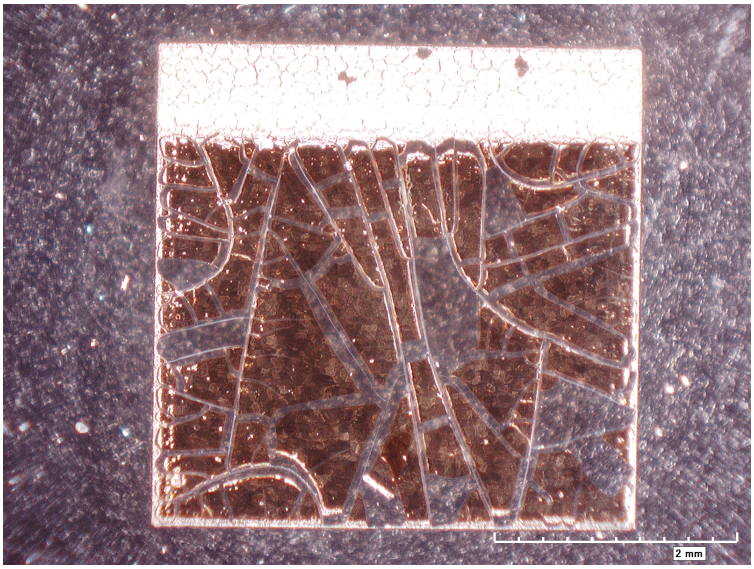

Figure 3.13: Cracking at higher temperatures (100°C)

3.3.3 Vacuum assisted drying

Five test samples were prepared as before (Section 3.3.2)under normal printing conditions (aluminum weigh cups used as the substrate). Samples were dried in a vacuum of 0.1 MPa for up to 4 hours with thickness and weight measurements recorded every hour. Most samples were either severely damaged or destroyed after the first two hours in vacuum. The samples that survived the 4 hours had shrunk by over 51% in thickness and 56% in weight (Table 3.21). Akin to air drying and heat assisted drying, vacuum assisted drying also aids evaporation of the liquid component of the printed electrolyte at the expense of surface quality.

Throughout the drying experiments described in Section 3.3, cracking was a consistent issue. The cracking usually begins 1 to 2 hours into the drying process and was typically exacerbated with the application of external heat and/or vacuum. After drying for more than 48 hours, most of these samples exhibit little or no cohesion to the substrate and readily dislodge from the substrate when the substrate is agitated. Samples printed on other substrates including glass, silicon and steel also exhibited the same behavior, insinuating that the mechanism of cracking with CeO_2 ink is substrate independent under similar vacuum conditions.

Table 3.21: Vacuum assisted drying: thickness and weight reduction at 0.1 MPa

Trial #	thickness (μm)		% diff	Starting	Weight (g) after elapsed time (hours)				% diff
	Starting	Ending		weight (g)	1	2	3	4	
1	14.75	6.80	53.90%	0.0017	0.0010	0.0009	0.0009	0.0007	58.82%
2	13.00	-	-	0.0015	0.0007	-	-	-	-
3	16.00	-	-	0.0018	0.0011	0.0009	-	-	-
4	16.50	-	-	0.0019	0.0010	0.0009	-	-	-
5	14.75	7.70	47.80%	0.0017	0.0008	0.0007	0.0007	0.0007	58.82%
6	15.75	8.00	49.21%	0.0018	0.0012	0.0010	0.0009	0.0008	55.56%
7	14.75	-	-	0.0017	0.0009	-	-	-	-
8	14.75	6.85	53.56%	0.0017	0.0012	0.0009	0.0008	0.0008	52.94%
9	13.75	-	-	0.0016	-	-	-	-	-
10	13.75	-	-	0.0016	-	-	-	-	-

Samples cured at vacuum levels of 0.05 - 0.02 MPa for 4 hours showed a visible reduction in the amount of cracking and damages along the surface of the test specimens. Adhesion to the print substrate, was extremely low with samples warping off the substrate after a time lapse of 48 hours. Extremely low vacuum levels (0.01 MPa and less) did not seem to produce any beneficial impact on the printed layers as well. While application of heat and/or vacuum seemed to slow down the rate at which test samples cracked, there was no evidence to support that either of these techniques were conducive to formation of a continuous layer of electrolyte.

Chapter 4

Conclusions

4.1 Summary of results

Printability of the nano-crystalline CeO_2 ink was established with two different ink formulations viz., the water based CeO_2 ink and the ethylene glycol based CeO_2 ink with suitable additives. Process parameters that influenced the response (thickness) of the printed layer/ film were identified and their ranges for hypothesis testing were established through pre-screening trials. The five (intrinsic) process parameters influencing film thickness were identified as atomizer flow rate, the flow rate differential between atomizer and virtual impactor (Δ), sheath flow rate, nozzle size and platen velocity. A five factor, two-level full factorial design was created for screening significant parameters for thickness. Investigation of the factorial design revealed Δ, nozzle size and platen velocity as significant with the response set as the square root of the thickness. A set of validation runs were performed to check for the existence of curvature within the design space. A regression model was fitted to the data after the residuals from the factorial analysis showed no abnormal results. Analysis of the residuals from the screening regression equation revealed a standard error (S statistic) of 0.569211 μm and a R-Sq value of 58% indicating that it could only account for 55% of the deviation. A higher order experiment was designed with just the significant parameters from screening to bring down the standard error. A three factor, three level (full factorial) design was executed and a new regression equation was obtained with a significantly lower spread of 0.0294616 μm and an increased R-Sq value (99.67%).

The increase in R-Sq values between the screening and higher order design experiments was attributed to external factors like the error resolution of the laser profilometer, overspray issues in the Optomec tool and presence of cracks on the surface of the printed samples. The updated regression equation obtained from Minitab was,

$$\mathrm{Sqrt(Height)} = 2.82534 + 0.290751\ (\Delta) + 0.424714\ (\text{nozzle size}) - 0.256312\ (\text{platen velocity})$$

A brief comparison of the coefficients of the regression equations from the screening and the higher order design of experiments is presented in Table 4.1.

Table 4.1: Comparison of coefficients of screening and updated regression equations

Term	Screening regression equation	Updated regression equation
Constant	2.8067	2.82534
Delta	0.305632	0.290751
Nozzle size	0.433245	0.424714
Platen velocity	-0.265175	-0.256312
R-Sq	55.35%	99.67%
Adjusted R-Sq	50.57%	99.62%
R-Sq (pred)	41.68%	99.54%
Standard error	0.569211	0.029462

The regression equations obtained from the screening and the higher order design of experiments was used for calculating predicted thicknesses for the verification runs and the center point runs. On analysis, it was revealed that the higher order regression equation reduced the deviation in predicted and actual thicknesses by 6%. Table 4.2 tabulates the measured deviations observed with the screening and regression equations calculated with and without the center point runs.

Table 4.2: Predicting thicknesses for verification runs: comparison of deviations

Regression equation	Without center point runs	With center point runs
Screening	$\pm$2.58%	$\pm$2.45%
Updated	$\pm$2.42%	$\pm$2.30%

A simple investigation of the drying method as an external factor influencing the printed electrolyte film was conducted. Test samples were printed on to aluminum cups and three drying methods were studied viz., air drying, heat assisted drying and vacuum drying. The study revealed that addition of external heat or vacuum to the system expedited the drying process and also helped reduce a higher percentage of liquid from the printed samples, as indicated by the measured weights after the drying cycles (see Table 4.3). However, cracking and poor substrate adhesion were noticed on many samples after the drying cycles. Cracking was also noticed to be exacerbated with the application of external heat or vacuum.

Table 4.3: Drying methods: summary of weight loss and shrinkage (%)

Drying method	Weight loss (%)	Layer thickness shrinkage (%)
Air	28%	30%
Heat	39%	40%
Vacuum	56%	51%

4.2 Future work

While the intrinsic process parameters for the Optomec Aerosol Jet system have been studied and modeled in this work, the effect of external factors on layer thickness needs further investigation. Varying the ink composition can lead to significant results, as surface chemistry would come into play. Drying methods investigated in this work need to be explored with a systematic approach, such as through design of experiments to establish conclusive results that can lead to minimized cracking on thin films. The data presented in such an analysis can be used in tandem with the data from this research to generate prediction algorithms with recommended parameter settings in the current design space, given a target layer thickness.

Sintering was found to not affect the structure of the printed layer during the feasibility study phase of this investigation; however the effect of sintering on the thickness of the printed layer has not been explored in this work. Increased temperatures during drying have caused a greater shrinkage in thickness as compared to room temperature (air) drying. Drying the printed layers at temperatures close to sintering temperatures can cause furthermore reduction in thickness and could possibly produce a denser film as well.

While slow drying (and slow sintering) have produced cracks in deposited films, the effect of rapid drying methods such as photonic sintering/ curing on cracking and layer thickness warrants inquiry. Photonic sintering systems are capable of delivering high power outputs onto a focused target area [42] and may have a beneficial impact on the layer width and reduce the cracking phenomenon. The entire cycle of drying, sintering and annealing happens within 10 milliseconds in the case of photonic sintering, thereby greatly reducing the chances of crack formations. Microwave based sintering has been successfully demonstrated with materials such as silver, yttria stabilized zirconia [43, 44] and is a candidate for study with ceria based electrolytes. Once process parameters for producing crack free thin layers of electrolyte are established, a complete solid oxide fuel cell can be assembled and tested for improvements in performance characteristics.

Self formed porosity in electrode structures

A promising investigation based on the results from the feasibility studies of this work is creating electrode structures for SOFCs where porosity in the layers is achieved by self-formed pore structures. Porosity is electrode structures is normally created and controlled by adding fugitive materials such as graphite, starch,etc., to the electrode structures and burning off the excessive materials via sintering [45]. Pores created by such methods tend to be irregularly shaped due to the shape of the fugitive materials themselves and the neck-like structures formed as a result do not represent a maximized triple phase boundary area. Observations made on the EDX analysis during the feasibility studies in this work show perfectly formed spheres of Ce in the microstructure. It is possible to control the rate of formation of these spheres and their distribution in a layer of material by manipulating ink chemistry and surface chemistry of the substrate. These could potentially be fabricated into electrode structures with well defined pores.

Trial experiments conducted with water based YSZ inks with ethylene glycol as co-solvent show varying increasing levels of porosity with increase in the ethylene glycol content in the ink. Understanding the mechanism of formation of these micro sized spheres and their response to changes in ink formulations and surface chemistry of substrates is worth investigating as it could lead to a potentially novel method of electrode fabrication for SOFCs that would reduce the number of post-processing steps significantly.

Figures 4.1 and 4.2 demonstrate the concept of porosity achieved by just Aerosol Jet deposition of YSZ ink followed by air drying. The test sample in Figure 4.2 was fabricated an ink with 20% YSZ, 70% distilled water and 10% ethylene glycol while the sample in Figure 4.1 was prepared with an ink with 20% YSZ and 80% distilled water. Clearly, the two samples show different porosity levels which appears to be linked to the ethylene glycol percentage in the ink.

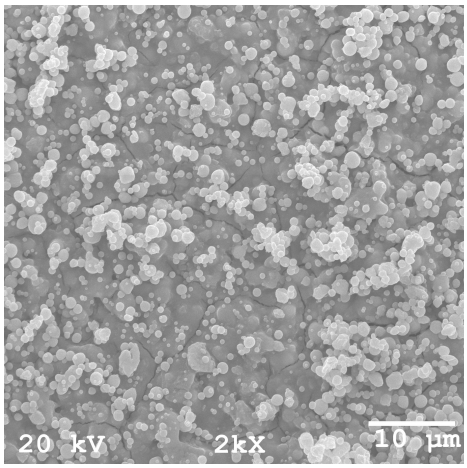

Figure 4.1: Porosity created with water based YSZ ink at 20% solid loading

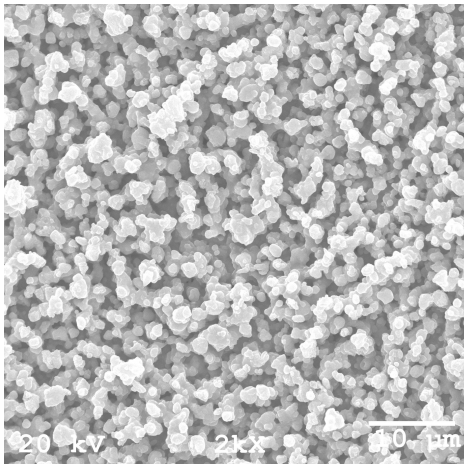

Figure 4.2: Porosity created with water based YSZ ink at 20% solid loading with 10% ethylene glycol

Bibliography

[1] J. Larminie, A. Dicks, and Knovel (Firm). Fuel cell systems explained. 2003.

[2] R.P. O'Hayre, S.W. Cha, and W. Colella. *Fuel cell fundamentals*. John Wiley & Sons, 2009.

[3] A. Wikeckowski and J. Norskov. *Fuel Cell Science: Theory, Fundamentals, and Biocatalysis*. The Wiley Series on Electrocatalysis and Electrochemistry. John Wiley & Sons, 2010.

[4] F. Tietz, H. P. Buchkremer, and D. Stöver. Components manufacturing for solid oxide fuel cells. *Solid State Ionics*, 152-153:373–381, December 2002.

[5] S.C. Singhal and M. Dokiya. *Solid oxide fuel cells VIII: (SOFC VIII) : proceedings of the International Symposium*. Number v. 8 in Proceedings (Electrochemical Society). Electrochemical Society, 2003.

[6] Toshio Suzuki, Toshiaki Yamaguchi, Yoshinobu Fujishiro, and Masanobu Awano. Fabrication and characterization of micro tubular sofcs for operation in the intermediate temperature. *Journal of Power Sources*, 160(1):73 – 77, 2006.

[7] S.C. Singhal and K. Kendall. *High temperature solid oxide fuel cells: fundamentals, design, and applications*. Electronics & Electrical. Elsevier, 2003.

[8] A. Boudghene Stambouli and E. Traversa. Solid oxide fuel cells (sofcs): a review of an environmentally clean and efficient source of energy. *Renewable and Sustainable Energy Reviews*, 6(5):433 – 455, 2002.

[9] Nguyen Q. Minh. Solid oxide fuel cell technology–features and applications. *Solid State Ionics*, 174(1-4):271 – 277, 2004. Solid State Ionics Dokiya Memorial Special Issue.

[10] Stephen J. Skinner. Recent advances in perovskite-type materials for sofc cathodes. *Fuel Cells Bulletin*, 4(33):6 – 12, 2001.

[11] SC Singhal. Science and technology of solid-oxide fuel cells. *Mrs Bulletin*, 25(3):16–21, 2000.

[12] WZ Zhu and SC Deevi. A review on the status of anode materials for solid oxide fuel cells. *Materials Science and Engineering A*, 362(1-2):228–239, 2003.

[13] S. Park, J.M. Vohs, and R.J. Gorte. Direct oxidation of hydrocarbons in a solid-oxide fuel cell. *Nature*, 404(6775):265–267, 2000.

[14] WZ Zhu and SC Deevi. Development of interconnect materials for solid oxide fuel cells. *Materials Science and Engineering A*, 348(1-2):227–243, 2003.

[15] Y. Matsuzaki and I. Yasuda. Dependence of SOFC cathode degradation by chromium-containing alloy on compositions of electrodes. *Journal of the Electrochemical Society(USA)*, 148(2), 2001.

[16] Ellen Ivers-TiffÃĹe, AndrÃĹ Weber, and Dirk Herbstritt. Materials and technologies for sofc-components. *Journal of the European Ceramic Society*, 21(10-11):1805 – 1811, 2001.

[17] Stephen W.Sophie. Nasa - home. john h. glenn research center, cleveland, ohio http://ntrs.nasa.gov/archive/nasa/casi.ntrs.nasa.gov/$20100011222_2010012665.pdf, 20Mar2011$.

[18] Nguyen Minh and Kurt Montgomery. Tape calendering manufacturing process for multilayer thin-film solid oxide fuel cells, 2004.

[19] D. Rotureau, J.-P. Viricelle, C. Pijolat, N. Caillol, and M. Pijolat. Development of a planar sofc device using screen-printing technology. *Journal of the European Ceramic Society*, 25(12):2633 – 2636, 2005. Elecroceramics IX.

[20] R.R. Flesner. Modeling of solid oxide fuel cell functionally graded electrodes and a feasibility study of fabrication techniques for functionally graded electrodes, 2009.

[21] R. Hui, Z. Wang, O. Kesler, L. Rose, J. Jankovic, S. Yick, R. Maric, and D. Ghosh. Thermal plasma spraying for sofcs: Applications, potential advantages, and challenges. *Journal of power sources*, 170(2):308–323, 2007.

[22] I. Zhitomirsky and A. Petric. Electrophoretic deposition of ceramic materials for fuel cell applications. *Journal of the European Ceramic Society*, 20(12):2055–2061, 2000.

[23] Y.M. Chiang, EB Lavik, I. Kosacki, HL Tuller, and JY Ying. Defect and transport properties of nanocrystalline ceo. *Applied physics letters*, 69:185, 1996.

[24] KS Brinkman, H. Takamura, HL Tuller, and T. Iijima. The oxygen permeation properties of nanocrystalline ceo thin films. *Journal of the Electrochemical Society*, 157:B1852, 2010.

[25] N. Sata, NY Jin-Phillipp, K. Eberl, and J. Maier. Enhanced ionic conductivity and mesoscopic size effects in heterostructures of baf2 and caf2. *Solid state ionics*, 154:497–502, 2002.

[26] S.F. Wang, Y.F. Hsu, C.H. Wang, and C.T. Yeh. Solid oxide fuel cells with sm0. 2ce0. 8o2-[delta] electrolyte film deposited by novel aerosol deposition method. *Journal of Power Sources*, 2011.

[27] AM Sukeshini, P. Gardner, F. Meisenkothen, T. Jenkins, R. Miller, M. Rottmayer, and T.L. Reitz. Aerosol jet printing and microstructure of sofc electrolyte and cathode layers. ECS, 2011.

[28] K.K.B. Hon, L. Li, and I.M. Hutchings. Direct writing technology–advances and developments. *CIRP Annals - Manufacturing Technology*, 57(2):601 – 620, 2008.

[29] Optomec - additive manufacturing technology; http://www.optomec.com/Additive-Manufacturing-Technology/Printed-Electronics. Accessed: 06/04/2011.

[30] A. Mette, PL Richter, M. Hörteis, and SW Glunz. Metal aerosol jet printing for solar cell metallization. *Progress in Photovoltaics: Research and Applications*, 15(7):621–627, 2007.

[31] J.H. Cho, J. Lee, Y. Xia, B.S. Kim, Y. He, M.J. Renn, T.P. Lodge, and C.D. Frisbie. Printable ion-gel gate dielectrics for low-voltage polymer thin-film transistors on plastic. *Nature materials*, 7(11):900–906, 2008.

[32] J. Akedo. Room temperature impact consolidation (rtic) of fine ceramic powder by aerosol deposition method and applications to microdevices. *Journal of Thermal Spray Technology*, 17(2):181–198, 2008.

[33] Optomec-material suppiers; http://www.optomec.com/Partners/Material-Suppliers. Accessed: 06/04/2011.

[34] G.H. Kang, J.P. Hong, G.T. Kim, and J.W. Park. Improved parameter modeling of interior permanent magnet synchronous motor based on finite element analysis. *Magnetics, IEEE Transactions on*, 36(4):1867–1870, 2000.

[35] R. Isermann. Process fault detection based on modeling and estimation methodsâĂŤa survey. *Automatica*, 20(4):387–404, 1984.

[36] Cerion Energy. Cerion energy - products; http://cerionenergy.com/articles/6. Accessed: 06/04/2011.

[37] Laser sensor il series http://www.keyence.com/dwn/il-ka.pdf. Accessed: 06/04/2012.

[38] D.C. Montgomery. *Design and Analysis of Experiments, Minitab Manual*. Student solutions manual. John Wiley & Sons, 2010.

[39] D.A. Powers and Y. Xie. *Statistical Methods for Categorical Data Analysis*. Emerald, 2008.

[40] T.B. Barker. *Quality by experimental design*, volume 43. CRC Press, 1994.

[41] ltd Imperial Chemical Industries. *Ethylene glycol*. Imperial chemical industries limited, 1938.

[42] K. Schroder. Pulse forge tools: enabling photonic curing for printed electronics. *Convertech & e-print*, 1(5):102–107, 2011.

[43] J. Perelaer, B.J. de Gans, and U.S. Schubert. Ink-jet printing and microwave sintering of conductive silver tracks. *Advanced materials*, 18(16):2101–2104, 2006.

[44] M.A. Janney, C.L. Calhoun, and H.D. Kimrey. Microwave sintering of solid oxide fuel cell materials: I, zirconia-8 mol% yttria. *Journal of the American Ceramic Society*, 75(2):341–346, 1992.

[45] P. Khatri-Chhetri. A novel approach to engineering structures of a solid oxide fuel cell (sofc): 3d direct write technology. 2011.

Appendix A

Sample Optomec code

Code for generating a 4mm x 4mm square (with no fill)

```
! *********************************
! FID1 0,0
! FID  END
! Generated by: Virtual Masking ÃE¸ Tools v1.84
! Axes: XYZTR=XY---
! Resolution: 4000,4000,-,-,-
! C:\Documents and Settings\OPTOMEC INC\Desktop\Toolpaths\Sundar\4x4square_100.dxf
! *********************************

ptp/e XY,20,20
OUT0.0=1
wait 3
MSEG XY,20,20
line XY,15980,20
line XY,15980,15980
```

```
line XY,20,15980
line XY,20,20
ENDS XY
till (^X_AST.#MOVE) & (^Y_AST.#MOVE)
OUT0.0=0

STOP
```

Appendix B

Minitab outputs

B.1 Distribution identification

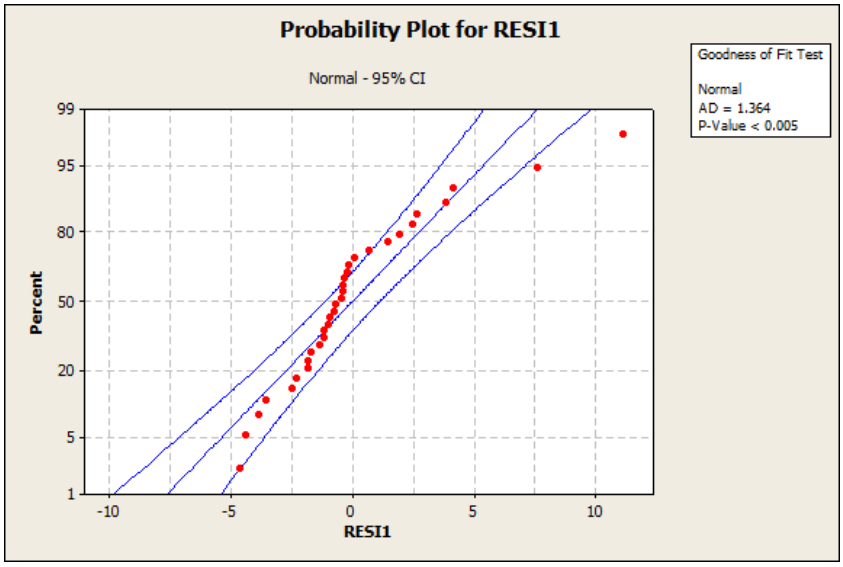

Figure B.1: Distribution identification for residuals of height

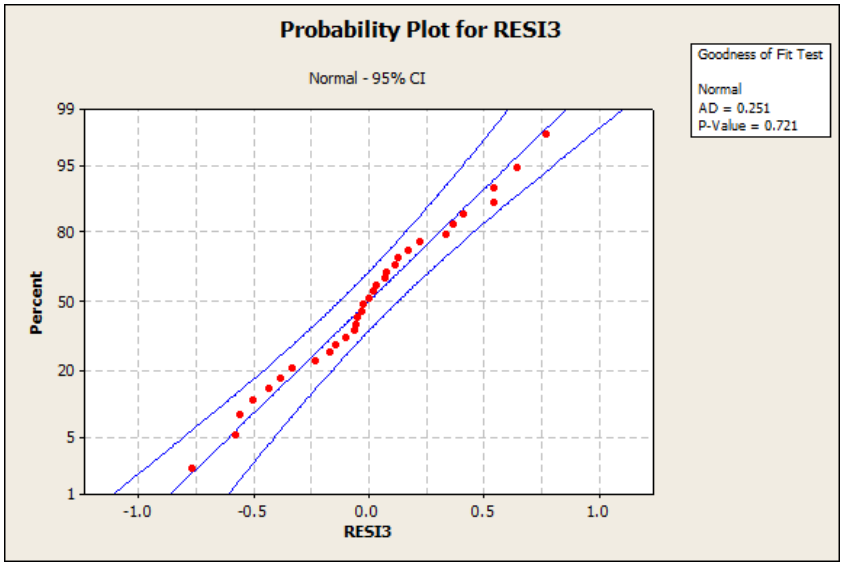

Figure B.2: Distribution identification for residuals of sqrt(height)

B.2 Factorial fit

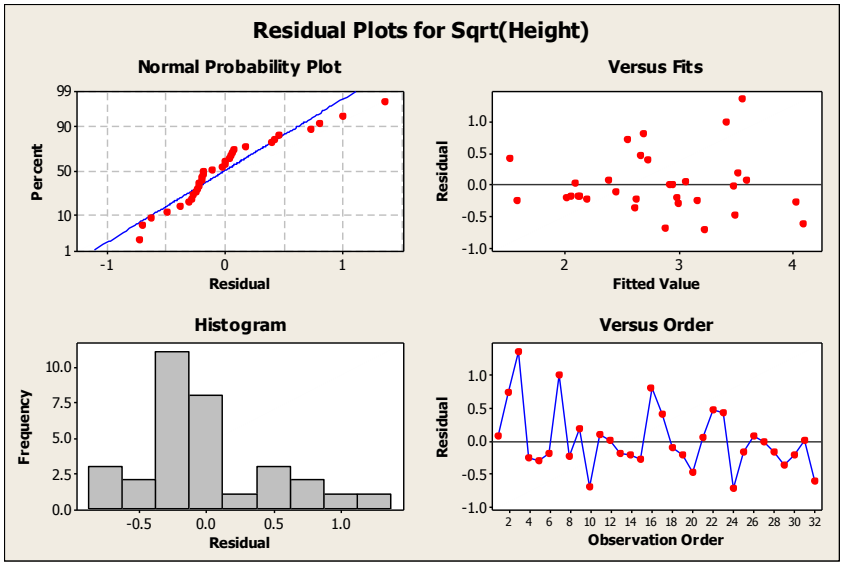

Figure B.3: Residual plots for Sqrt(Height): interactions up to second order

Factorial Fit: Sqrt(Height) versus Atomizer, Delta, ...

Estimated Effects and Coefficients for Sqrt(Height) (coded units)

Term	Effect	Coef	SE Coef	T	P
Constant		2.8067	0.09057	30.99	0.000
Atomizer	0.0679	0.0340	0.09057	0.37	0.713
Delta	0.6113	0.3056	0.09057	3.37	0.004
Sheath	-0.4991	-0.2495	0.09057	-2.76	0.014
Nozzle	0.8665	0.4332	0.09057	4.78	0.000
Platen Velocity	-0.5304	-0.2652	0.09057	-2.93	0.010
Atomizer*Delta	0.2781	0.1390	0.09057	1.54	0.144
Atomizer*Sheath	-0.1116	-0.0558	0.09057	-0.62	0.546
Atomizer*Nozzle	0.1363	0.0682	0.09057	0.75	0.463
Atomizer*Platen Velocity	0.4163	0.2082	0.09057	2.30	0.035
Delta*Sheath	0.1129	0.0564	0.09057	0.62	0.542
Delta*Nozzle	-0.0093	-0.0046	0.09057	-0.05	0.960
Delta*Platen Velocity	0.1929	0.0964	0.09057	1.06	0.303
Sheath*Nozzle	-0.0579	-0.0290	0.09057	-0.32	0.753
Sheath*Platen Velocity	-0.1388	-0.0694	0.09057	-0.77	0.455
Nozzle*Platen Velocity	-0.0316	-0.0158	0.09057	-0.17	0.864

S = 0.512327 PRESS = 16.7986
R-Sq = 79.33% R-Sq(pred) = 17.32% R-Sq(adj) = 59.95%

Analysis of Variance for Sqrt(Height) (coded units)

Source	DF	Seq SS	Adj SS	Adj MS	F	P
Main Effects	5	13.2754	13.2754	2.65508	10.12	0.000
Atomizer	1	0.0369	0.0369	0.03691	0.14	0.713
Delta	1	2.9892	2.9892	2.98915	11.39	0.004
Sheath	1	1.9927	1.9927	1.99273	7.59	0.014
Nozzle	1	6.0064	6.0064	6.00644	22.88	0.000
Platen Velocity	1	2.2502	2.2502	2.25017	8.57	0.010
2-Way Interactions	10	2.8427	2.8427	0.28427	1.08	0.428
Atomizer*Delta	1	0.6186	0.6186	0.61855	2.36	0.144
Atomizer*Sheath	1	0.0996	0.0996	0.09964	0.38	0.546
Atomizer*Nozzle	1	0.1486	0.1486	0.14864	0.57	0.463
Atomizer*Platen Velocity	1	1.3866	1.3866	1.38664	5.28	0.035
Delta*Sheath	1	0.1019	0.1019	0.10190	0.39	0.542
Delta*Nozzle	1	0.0007	0.0007	0.00069	0.00	0.960
Delta*Platen Velocity	1	0.2976	0.2976	0.29760	1.13	0.303
Sheath*Nozzle	1	0.0269	0.0269	0.02685	0.10	0.753
Sheath*Platen Velocity	1	0.1542	0.1542	0.15421	0.59	0.455
Nozzle*Platen Velocity	1	0.0080	0.0080	0.00800	0.03	0.864
Residual Error	16	4.1997	4.1997	0.26248		
Total	31	20.3178				

Unusual Observations for Sqrt(Height)

Obs	StdOrder	Sqrt(Height)	Fit	SE Fit	Residual	St Resid
3	28	4.92443	4.15302	0.36227	0.77141	2.13R
25	5	1.87083	2.63860	0.36227	-0.76777	-2.12R

R denotes an observation with a large standardized residual.

Half Normal Effects Plot for Sqrt(Height)

Alias Structure
I
Atomizer
Delta
Sheath
Nozzle
Platen Velocity
Atomizer*Delta
Atomizer*Sheath
Atomizer*Nozzle
Atomizer*Platen Velocity
Delta*Sheath

B.3 Regression analysis: screening

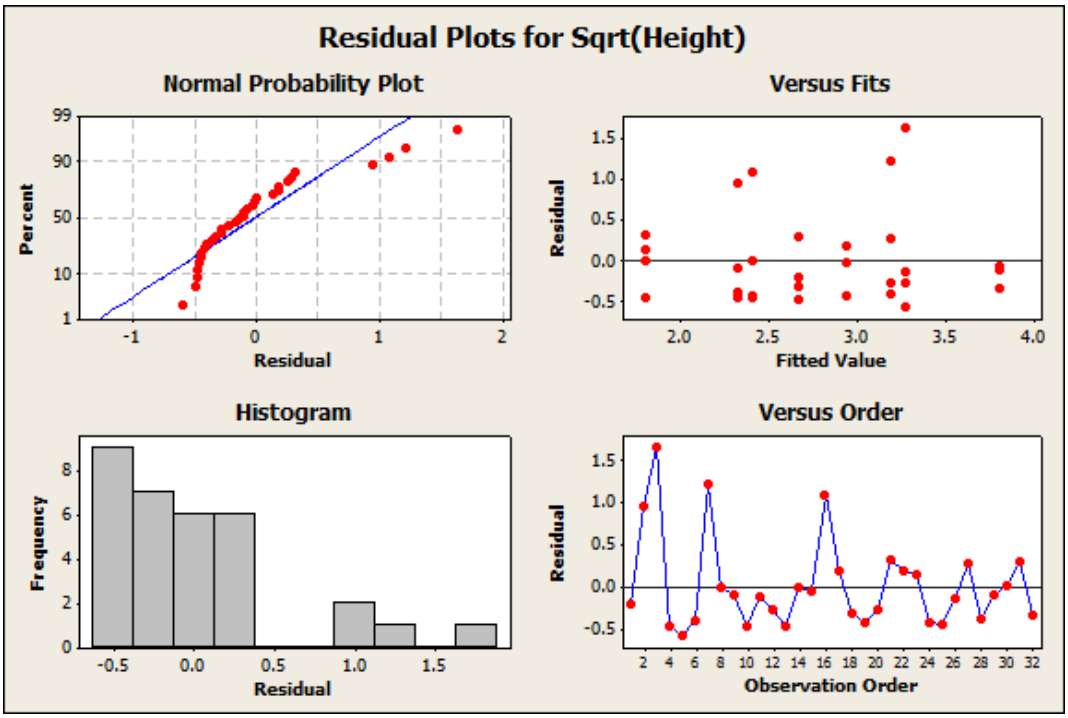

Figure B.4: Residual plots for regression analysis of reduced model

General Regression Analysis: Sqrt(Height) versus Delta, Nozzle, Platen Velocity

Regression Equation

Sqrt(Height) = 2.8067 + 0.305632 Delta + 0.433245 Nozzle - 0.265175 Platen Velocity

Coefficients

Term	Coef	SE Coef	T	P
Constant	2.80670	0.100623	27.8932	0.000
Delta	0.30563	0.100623	3.0374	0.005
Nozzle	0.43324	0.100623	4.3056	0.000
Platen Velocity	-0.26518	0.100623	-2.6353	0.014

Summary of Model

S = 0.569211 R-Sq = 55.35% R-Sq(adj) = 50.57%
PRESS = 11.8492 R-Sq(pred) = 41.68%

Analysis of Variance

Source	DF	Seq SS	Adj SS	Adj MS	F	P
Regression	3	11.2458	11.2458	3.74859	11.5697	0.000041
Delta	1	2.9892	2.9892	2.98915	9.2258	0.005120
Nozzle	1	6.0064	6.0064	6.00644	18.5383	0.000184
Platen Velocity	1	2.2502	2.2502	2.25017	6.9450	0.013547
Error	28	9.0720	9.0720	0.32400		
Lack-of-Fit	4	0.5033	0.5033	0.12584	0.3525	0.839728
Pure Error	24	8.5687	8.5687	0.35703		
Total	31	20.3178				

Fits and Diagnostics for Unusual Observations

Obs	Sqrt(Height)	Fit	SE Fit	Residual	St Resid	
3	4.92443	3.28040	0.201246	1.64403	3.08767	R
7	4.41588	3.19949	0.201246	1.21639	2.28453	R
16	3.50000	2.41391	0.201246	1.08609	2.03980	R

R denotes an observation with a large standardized residual.

B.4 Regression analysis: higher order design

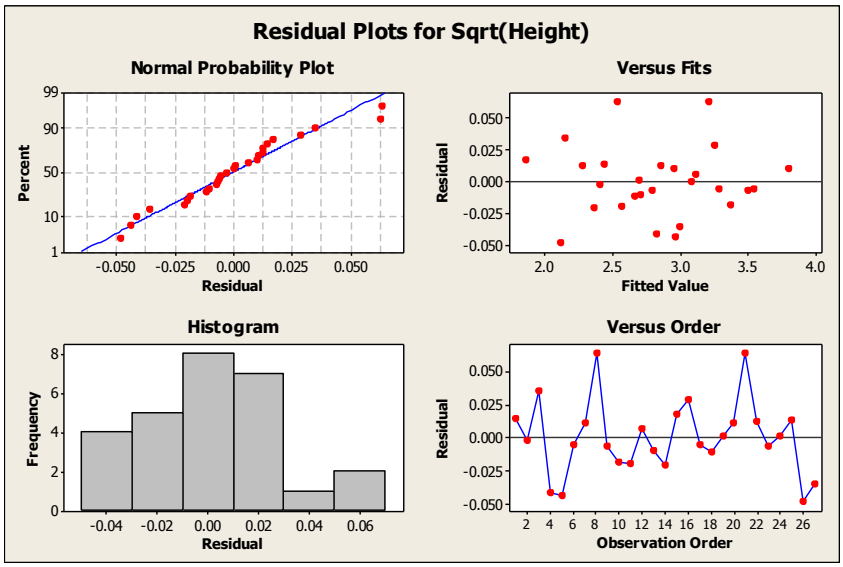

Figure B.5: Residual plots for regression analysis of higher order design

General Regression Analysis: Sqrt(Height) versus Delta, Nozzle Size, ...

Regression Equation

Sqrt(Height) = 2.82534 + 0.290751 Delta + 0.424714 Nozzle Size - 0.256312 Platen Velocity

Coefficients

Term	Coef	SE Coef	T	P
Constant	2.82534	0.0056699	498.306	0.000
Delta	0.29075	0.0069442	41.870	0.000
Nozzle Size	0.42471	0.0069442	61.161	0.000
Platen Velocity	-0.25631	0.0069442	-36.910	0.000

Summary of Model

S = 0.0294616 R-Sq = 99.67% R-Sq(adj) = 99.62%
PRESS = 0.0271856 R-Sq(pred) = 99.54%

Analysis of Variance

Source	DF	Seq SS	Adj SS	Adj MS	F	P
Regression	3	5.95105	5.95105	1.98368	2285.39	0
Delta	1	1.52165	1.52165	1.52165	1753.08	0
Nozzle Size	1	3.24688	3.24688	3.24688	3740.71	0
Platen Velocity	1	1.18252	1.18252	1.18252	1362.37	0
Error	23	0.01996	0.01996	0.00087		
Total	26	5.97102				

Fits and Diagnostics for Unusual Observations

Obs	Sqrt(Height)	Fit	SE Fit	Residual	St Resid	
8	2.59808	2.53459	0.0089649	0.0634858	2.26214	R
21	3.27872	3.21562	0.0132971	0.0631030	2.40025	R

R denotes an observation with a large standardized residual.